

**SINGLE NANOPARTICLE SENSING WITH  
NANOELECTROMECHANICAL  
RESONATORS OPERATING AT  
NONLINEAR REGIME**

A THESIS SUBMITTED TO  
THE GRADUATE SCHOOL OF ENGINEERING AND SCIENCE  
OF BILKENT UNIVERSITY  
IN PARTIAL FULFILLMENT OF THE REQUIREMENTS FOR  
THE DEGREE OF  
MASTER OF SCIENCE  
IN  
MECHANICAL ENGINEERING

By  
Mert Yüksel  
August 2019

Single Nanoparticle Sensing with Nanoelectromechanical Resonators  
Operating at Nonlinear Regime  
By Mert Yüksel  
August 2019

We certify that we have read this thesis and that in our opinion it is fully adequate,  
in scope and in quality, as a thesis for the degree of Master of Science.

---

Mehmet Selim Hanay(Advisor)

---

Alper Demir

---

Barbaros Çetin

Approved for the Graduate School of Engineering and Science:

---

Ezhan Kardeşan  
Director of the Graduate School

# ABSTRACT

## SINGLE NANOPARTICLE SENSING WITH NANOELECTROMECHANICAL RESONATORS OPERATING AT NONLINEAR REGIME

Mert Yüksel

M.S. in Mechanical Engineering

Advisor: Mehmet Selim Hanay

August 2019

Machines working at the nanoscale dimensions offer an important technological opportunity for healthcare and biomedical screening. State-of-the-art nanomachines are usually operated at small displacements, since engineering tools for their control at large vibration amplitudes have so far been absent. Nanoelectromechanical Systems (NEMS) have emerged as a promising technology for performing the mass spectrometry of large biomolecules and nanoparticles. Nanoparticles constitute an important family in the nanotechnology toolbox, because they indicate potential pollutions early on, or can be designed to act as drug carriers for cancer therapy. As nanoscale objects land on NEMS sensor one by one, they induce resolvable shifts in the resonance frequency of the sensor proportional to their weight. The operational regime of NEMS sensors is often limited by the onset-of-nonlinearity, beyond which the highly sensitive schemes based on frequency tracking by phase-locked loops cannot be readily used. Here, we develop a measurement architecture to operate at the nonlinear regime and measure frequency shifts induced by analytes in a rapid and sensitive manner. We used this architecture to individually characterize the mass of gold nanoparticles and verified the results by performing independent measurements of the same nanoparticles based on linear mass sensing. Once the feasibility of the technique is established, we have obtained the mass spectrum of a 20 nm gold nanoparticle sample by individually recording about five hundred single particle events using two modes working sequentially in the nonlinear regime. The technique obtained here can be used for thin nanomechanical structures which possess a limited dynamic range.

*Keywords:* NEMS, Nonlinear Sensing, Gold Nanoparticles, Mass Spectrometry, Nanoparticle Detection, Nanomechanical Sensors.

## ÖZET

# DOĞRUSAL OLMAYAN REJİMDE ÇALIŞAN NANOELEKTROMEKANİK REZONATÖRLERLE TEK Lİ NANOPARÇACIK ALGILAMA

Mert Yüksel

Makine Mühendisliği, Yüksek Lisans

Tez Danışmanı: Mehmet Selim Hanay

Ağustos 2019

Nano boyutta çalışan makineler, sağlık ve biyomedikal tarama için önemli bir teknolojik fırsat sunmaktadır. En son teknolojiye sahip bu nano makineler, geniş titreşim genliklerinde kontrolü için mühendislik araçları mevcut olmadığından dolayı genellikle küçük titreşim genliklerinde çalıştırılır. Nanoelektromekanik Sistemler (NEMS), büyük biyomoleküller ve nanopartiküllerin kütle spektrometrisini gerçekleştirmek için umut verici bir teknoloji olarak ortaya çıkmıştır. Nanopartiküller, nanoteknoloji alanında büyük bir öneme sahiptir, çünkü bunlar erken dönemde potansiyel kirlenmeleri göstermek veya kanser tedavisi için ilaç taşıyıcı olarak görev yapmak için kullanılabilir. Nano boyuttaki nesnelere NEMS sensörüne tek tek indiğinde, sensörün rezonans frekansında ağırlıklarına orantılı olarak çözülebilir kaymalar yaratırlar. NEMS sensörlerinin çalıştığı aralık, genellikle faz kilitli döngülerin frekans izlemesine dayanan yüksek hassasiyetli şemaların kolayca kullanılmadığı, nonlineerite başlangıcı ile sınırlıdır. Bu çalışmada, lineer olmayan rejimde çalışarak ve nano parçacıkların sebep olduğu frekans kaymalarını hızlı ve hassas bir şekilde ölçmek için bir ölçüm mimarisi geliştirdik. Altın nano partiküllerin kütlelerini tek tek karakterize etmek için bu mimariyi kullandık ve aynı nanopartiküllerin lineer kütle algılamaya dayalı bağımsız ölçümlerini yaparak sonuçları doğruladık. Tekniğin uygulanabilirliği test edildikten sonra, doğrusal olmayan rejimde sıralı olarak çalışan iki modu kullanarak yaklaşık beş yüz nano parçacığı ayrı ayrı inceleyerek 20 nm altın nanoparçacık numunesinin kütle spektrumunu elde ettik. Burada kullanılan teknik sınırlı bir dinamik aralığa sahip olan küçük nanomekanik yapılar için kullanılabilir.

*Anahtar sözcükler:* NEMS, Doğrusal Olmayan Algılama , Altın Nano Parçacıklar, Kütle Spektrometrisi, Nano Parçacık Algılama, Nanomekanik Sensörler.

# Acknowledgement

I feel very privileged to work with Dr. Selim Hanay for many reasons. His support and guidance in academia and also in life helped me get through all the difficulties that I encountered in this process. I believe it is hard to find an advisor who wants the best for his student more than himself and this is what makes Dr. Selim Hanay one of a kind. His kindness, support, and intelligence motivated me to work harder. I will always appreciate the values he has given me and one day I hope to become as successful as he is.

I would like to thank my thesis committee, Prof. Alper Demir for his valuable discussions and ideas, also Assoc. Prof. Barbaros Çetin for his contributions throughout my undergraduate and graduate education. I also thank both of them for their valuable time in my thesis defense.

I would like to express my gratitude for Prof. Adnan Akay and Assoc. Prof. Ilker Temizer for their assistance and recommendation letters for my PhD applications.

I am very proud to be a son of my parents, Dilek and Halil. Their unconditional love and support have always been with me in every move I make in life and I will always feel this connection in every part of my life. I am very grateful for having a little sister, Deniz, who has always given me a smile since the day she was born. A special friend who makes the life more bearable in hard times and more delightful in good times is a precious value to have. I thank Dulce for being that person to me. I cherish Ozan for his sincere and honest friendship that always boosts my motivation. I thank Müge for her great company in every times. I appreciate Cem and Murat for the joy they always bring with their stories and absurdities. I thank Orhun for his big comebacks in delicate moments. I thank Gökhan and Özge for their lasting friendships since our childhood.

I would like to thank all the friends that I met in Hanay Group for their sympathetic and valuable conversations and their supports. Thank you Hande for

being very close friend of mine and thank you Kelleci for being the extraordinary desk mate for me. I thank Atakan and Çağatay for their help when I first joined the group. I appreciate all the work we have done together with Ezgi. I thank Selçuk for being a great roommate in every conferences. I thank Utku for his valuable and logical discussions. I also thank Hakan and Tufan for their help when needed.

This work was supported by the Scientific and Technological Research Council of Turkey (TÜBİTAK). We acknowledge support from TÜBA and Bilim Akademisi.

# Contents

- 1 Introduction** **1**
  - 1.1 Nanoelectromechanical System Resonators . . . . . 1
  - 1.2 Mass Sensing with NEMS Resonators . . . . . 2
  - 1.3 Thesis Outline . . . . . 3
  
- 2 Nanoelectromechanical Resonators and Mass Spectrometry Applications** **5**
  - 2.1 Fabrication and Characterization of NEMS Resonators . . . . . 5
  - 2.2 Motion in NEMS Resonators . . . . . 8
  - 2.3 Motivation for Mass Sensing in Nonlinear Regime . . . . . 12
  
- 3 A Method for Nonlinear Sensing: Trajectory Locked Loop (TLL)** **16**
  - 3.1 Introducing TLL . . . . . 17
  - 3.2 Controller Design . . . . . 22
  - 3.3 Frequency Fluctuations in Nonlinear Regime . . . . . 29

|          |  |           |
|----------|--|-----------|
| 3.4      | Sequential TLL for Two Mode Sensing . . . . .          | 33        |
| <b>4</b> | <b>Single Nanoparticle Sensing in Nonlinear Regime</b> | <b>35</b> |
| 4.1      | Experimental Setup . . . . .                           | 35        |
| 4.2      | Two Mode Sensing with Sequential TLL . . . . .         | 37        |
| 4.3      | Mass Spectrometry of 20nm Gold Nanoparticles . . . . . | 40        |
| <b>5</b> | <b>Concluding Remarks</b>                              | <b>46</b> |
| <b>A</b> | <b>Matlab Code for TLL</b>                             | <b>55</b> |
| <b>B</b> | <b>Matlab Code for Sequential TLL</b>                  | <b>59</b> |

# List of Figures

|     |   |   |
|-----|---|---|
| 1.1 | A single nanoparticle landing on a nanomechanical resonator causes a frequency shift at the resonance frequency. This phenomena is used for mass sensing. . . . .   | 3 |
| 2.1 | Fabrication steps of the doubly clamped beam nanomechanical resonators. . . . .   | 6 |
| 2.2 | (a) In our design, one chip has 9 devices in variety of lengths. (b) 1 device has 5 contact pads that are used for actuation and detection of the resonance motion. (c,d) Bridge Silicon nitride resonator is demonstrated in different angles. Gold electrodes at the clamped ends are designed to reach less than %5 of the beam's total lenght not to disrupt the resonance mode shapes. White bar represents 300,100,5,2 micron respectively. . . . . | 7 |
| 2.3 | Transduction scheme of the NEMS resonator. Actuation and detection of the motion are obtained by the transducers which convert the mechanical motion to electrical signal and vica versa. . . . .   | 9 |

2.4 (a) SEM image of the doubly clamped beam resonator used for thermoelastic actuation and piezoresistive detection. (b) Materials are indicated for the resonator. (c,d) Thermoelastic actuation scheme with AC drive (a) and AC+DC drive(d). For the AC drive resonance condition is reached when  $\omega_{drive} = \frac{\omega_n}{2}$  and for the AC+DC drive; resonance is reached when  $\omega_{drive} = \omega_n$ . (c) and (d) are recreated from [1] . . . . . 10

2.5 (a) SEM image of the 20  $\mu m$  doubly-clamped beam resonator used in the experiments. The scale bar is 5 micron. (b) Actuation and detection scheme implemented for the NEMS resonator are demonstrated. Simplicity of the electronic circuit allows feasible experimentation of the proposed method. . . . . 11

2.6 First resonance mode of the NEMS resonator obtained by thermoelastic actuation and piezoresistive detection methods. (a) Amplitude and (b) phase responses are measured with the HF2LI Lock in amplifier. Quality factor of the given mode is calculated as 12000 while the resonance frequency is at 12.567 MHz. . . . . 12

2.7 (a) Nonlinear regime provides better signal and wider operational range for NEMS resonators. (b)Linear dynamic range for several doubly clamped beam resonators. The shaded region indicates the absence of a linear regime. Figure is recreated from [2]. . . . . 14

- 3.1 Linear and nonlinear response of the NEMS resonator (a,b) In the linear regime, a sharp phase transition is observed with the quality factor of 12000.  $0^\circ$  crossing in phase can be used as a reference target for PLL. The inset shows the SEM image of a typical doubly-clamped beam resonator used in the experiments. The scale bar is 3 micron. (c,d) The resonator acts as a ideal Duffing resonator with a positive Duffing term when it is driven with larger excitations. Nonlinear phase jumps are observed depending on the sweep direction (blue and orange data points for the sweep from left to right and from right to left respectively).  $f_{up}$  and  $f_{down}$  frequencies are defined at the boundaries of the hysteresis window. In the colored area, the resonator shows a bistable response.  $0^\circ$  phase cannot be locked with the PLL as it is in the unstable region of the nonlinear response. . . . . 18
- 3.2 Trajectory Locked Loop (TLL). (a) The controller is adjusted for highly sensitive measurements of bifurcation frequencies. Circle data points show the frequency sweep steps which becomes denser while getting closer to the boundaries. (b) The one full cycle indicated with a red rectangle in (a) is maximized and plotted with the corresponding phase response. It is possible to extract  $f_{u-p}$  and  $f_{down}$  at the points where the phase jumps with a near infinite slope as they are indicated with red circles. For the given case, notice that one cycle approximately takes 0.6 seconds which can be comparable with many of the PLLs used in this field. (c) The projection of the TLL over time is displayed. It can be clearly seen that TLL holds the nonlinear resonator inside the hysteresis window. 20

|     |  |    |
|-----|--|----|
| 3.3 | (a) Nonlinear phase response of the resonator is demonstrated with the boundaries of the bistable regime. $\phi_{up}$ is the phase value right before the jump takes place while sweeping from left to right and vice versa for $\phi_{down}$ . (b) Controller design for the TLL. $\phi_{up}$ and $\phi_{down}$ are used to adjust the total gain in the system: gain is decreased when the phase response of the resonator is getting closer to one of the thresholds, therefore frequency steps are also reduced for more accurate measurement of the $f_{up}$ and $f_{down}$ . NCO stands for Numerically Controlled Oscillator. . . . . | 22 |
| 3.4 | (a) TLL performed with 35ms loop time. Red lines indicate the recorded $f_{down}$ points and the black arrows are used to indicate the same time interval between 2 measurements. (b) Frequency shifts due to gold nanoparticles are captured with the fast TLL time (100ms). . . . .  | 25 |
| 3.5 | (a) One TLL cycle inside the hysteresis window, as it is also used in Figure 3.2b in the main text. (b) Red rectangle in (a) is zoomed for better realization of the small frequency step (4 Hz) just before phase jump. . . . .   | 26 |
| 3.6 | Amplitude response, phase response and TLL operation are demonstrated from top to bottom for three different SBR. . . . .  | 28 |
| 3.7 | (a) Jump frequencies ( $f_{up}$ and $f_{down}$ ) are extracted from TLL operation. (b) Time trace is captured with the frequency and then later used for Allan deviation calculation. . . . .  | 30 |

- 3.8 Frequency instabilities for the first mode frequency in nonlinear regime is investigated at different drive powers. The actuation voltage is increased from (a) to (d). Allan deviations at the linear regime (dark grey line) are compared with fluctuations at  $f_{up}$  (blue line) and  $f_{down}$  (orange line). The nonlinear drive voltage levels for a-d are: 75, 85, 95, 115mV respectively (half-omega drive is used). We note that the cycle time of the TLL was 1 seconds; however, noise statistics should be reported starting from 50ms averaging time scale as it is the duration between each point within the cycle. With 50ms duration between each point, the first data on the Allan deviation plot occurs for a 50ms averaging time and a 950ms dead time. Owing to the overall white FM characteristics, the dead time does not play a significant role. . . . . 31
- 3.9 Frequency instabilities for the second mode frequency in nonlinear regime is investigated with the same method mentioned in Figure 3.8. The nonlinear drive power levels for a-d are : 112.5, 122.5, 125, 140 mV respectively (half-omega drive is used). . . . . 32
- 3.10 First and second resonance modes are tracked by TLL sequentially in order to minimize coupling between two nonlinear modes. After one mode completes the one full cycle inside the hysteresis window, the other mode is driven by TLL. . . . . 34
- 4.1 (a) Schema of Experimental setup from top view. (b) Photograph of the experimental setup used for MALDI of gold nanoparticles. . . . . 36

4.2 Comparison of nano particle induced frequency shifts in nonlinear and linear regime. (a) PLL and TLL are performed consecutively by sequentially switching between the operation regimes. PLL time is set to approximately 4s (shaded green) while the TLL is performed for one full cycle of the first and second mode (shaded grey). (b) While driving the resonator with these technique, 20 nm gold nanoparticle induced frequency shifts are captured for the first two modes of the resonator in linear (solid lines with black (first mode) and purple (second mode)) and nonlinear regime (circle data points with blue (first mode) and orange (second mode)) via PLL and TLL respectively. The TLL frequency jumps are calculated by considering the lowest data point in each cycle, which corresponds to  $f_{down}$ . . . . . 38

4.3 Single nano particle induced fractional frequency shifts are obtained in nonlinear regime by measuring the shifts in  $f_{down}$  and they are compared with the linear fractional shifts for the same particle as it is observed in Figure 4.2 . . . . . 39

4.4 Gold nanoparticle (GNP) sensing with Sequential TLL. The frequency shifts due to individual GNP deposition. Each GNP adsorption causes frequency shifts in both modes, which emerge as sudden shifts in the trajectories (inset). . . . . 40

4.5 (a) Mass spectrometry of 20 nm gold nanoparticles. (b) Diameter is calculated with the bulk density of gold ( $\rho_{Au} = 19.3\text{g/cm}^3$ ). Orange-shaded regions illustrate the detection criterion due to frequency fluctuations of the nonlinear resonator used in the experiments (by assuming the responsivity of the first mode and considering a particle landing at the very center). . . . . 41

4.6 SEM images of the 20 micron doubly-clamped beam resonator used for nonlinear mass spectra before (a) and after (b) MALDI process of the gold nanoparticles. Scale bar is 5 micron. . . . . 42

4.7 Dynamic range comparison between linear and nonlinear regime for mass sensing with PLL and TLL. . . . . 43

4.8 An instance when the first mode PLL fails due to a large frequency shift around  $t = 7s$ . (a) PLL simultaneously tracks the first and second mode frequencies in the linear regime. Arrow indicates the moment when the particle lands. Second mode PLL stays phase locked while the first mode PLL fails. (b) Phase response during PLL. After failure for the first mode, phase response is kicked out of the resonance phase transition which results in high errors. . . 44

4.9 Two different instances where TLL detects frequency shifts much larger than the linear bandwidth of the resonator, for the (a) first, and (b) second modes. . . . . 44

4.10 Nonlinear and linear mass spectrum are compared. Nonlinear data is the same with the Figure 4.5. Mass spectra (a) and diameter spectra (b) with the assumption of bulk gold density are provided. 45

4.11 Results from linear and nonlinear mass spectrum. . . . . 45

# Chapter 1

## Introduction

### 1.1 Nanoelectromechanical System Resonators

Improvements in the fabrication of micro and nano scale structures have allowed the development of nanoelectromechanical systems (NEMS). Particularly, NEMS resonators have been used as exquisite sensors of physical stimuli thanks to their high responsivity, fast response, and accessible actuation and detection. As the size of a mechanical sensor shrinks, its responsivity increases. Combining this advantage with low-noise readout schemes has enabled extreme sensitivity levels to be achieved, such as the detection of electronic spins [3], single-atoms [4], single-proteins [5, 6], nanoparticles [7, 8], and single-cells in liquid [9, 10]. A novel sensing modality of NEMS technology for single-molecule analysis has been discovered recently. It was shown that the spatial properties of analyte particles, such as their size and skewness, can be extracted by using multiple mechanical modes of a sensor [11]. Such multimodal measurements provide both size and shape features, as well as the mass of the analyte. Furthermore, by merging different spatial features, an image of the analyte can be reconstructed. The new technique, inertial imaging [11], transforms the capabilities of nanomechanical sensors to a new level: the combined data of molecular mass, size and shape

of the analyte can provide previously unattainable insights in biomolecular analytics. The technique can be used for any resonator system with well-defined mode shapes: for instance, the electromagnetic analog of inertial imaging was also demonstrated in a microfluidic environment using microwave sensors [12].

In the last decade, interest in the nonlinear dynamics of the nanomechanical resonators has grown rapidly. Nonlinearity is readily available in these resonators due to their small geometry and low dissipation [13]. Consequently, the study of nonlinear behavior of nanomechanical resonators became a practical need to understand the fundamentals of nonlinear dynamics and avoid or exploit it efficiently when it is desired. Although nonlinear regime is easily achievable with nanomechanical resonators, unfortunately there is not much work done at nonlinear regime on the contrary of linear regime. This is because linearity is easier to understand and work on and there are already available softwares (such as Phase Locked Loop (PLL) systems) for the linear resonators. However, advantages of nonlinearity in NEMS resonators are yet to be discovered.

## 1.2 Mass Sensing with NEMS Resonators

Cantilever and doubly clamped beam structures are widely used as a nanomechanical resonators. Motion in these resonators can easily be modeled as a mass spring damper system, which is explained in more details in Chapter 2. Thanks to their high frequency and high quality factors, NEMS resonators are very sensitive to external disturbances. In mass sensing, a single nanoparticle can be considered as an external disturbance. When a single particle lands on a resonator, it causes a frequency shift at the resonance modes of the resonator (Figure 1.1) depending on its mass, landing position, and geometry. These frequency shifts can be detected with the highly sensitive detection methods, which are discussed in Chapter 2. By obtaining the frequency shifts in multiple modes, it is possible to extract information about the single nanoparticle that lands on a NEMS resonator [11].

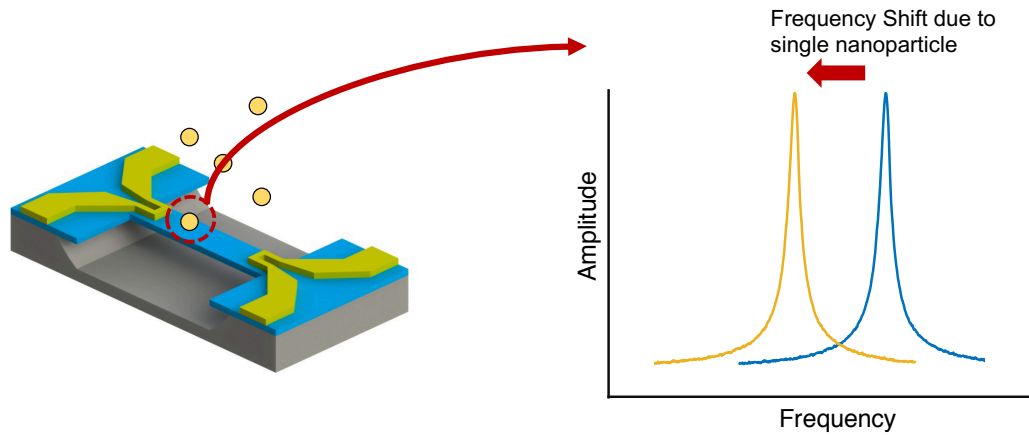


Figure 1.1: A single nanoparticle landing on a nanomechanical resonator causes a frequency shift at the resonance frequency. This phenomena is used for mass sensing.

Mass sensing aims to measure the molecular weight of a single nano particle. At the nano scale, investigation of individual proteins and viruses have been an important subject for characterization of different biological molecules. Although NEMS resonators give a great promise to be used as a tool for single molecule detection, the methods that are used for sensing have still been developing. Controller systems that track the resonance frequency to measure the frequency shifts due to single nanoparticles are very well developed for the linear response of the NEMS resonators. However, there is not a convenient method developed for sensing at nonlinear regime. In this work, we show mass sensing at the nonlinear regime with the method that we have developed.

### 1.3 Thesis Outline

In this work, mass spectrometry with NEMS resonators working at nonlinear regime is demonstrated for the first time. Chapter 2 gives a brief introduction to NEMS technology and its mass sensing applications. Detailed information on

nanoelectromechanical resonators is provided. Fabrication process, mathematical analysis of motion in these resonators, actuation and detection methods, and finally the motivation for nonlinear sensing are explained.

Chapter 3 presents a robust method that is developed and used for the first time for nonlinear sensing. The method is called Trajectory Locked Loop (TLL) and designed to track the bifurcation frequencies at the nonlinear regime. It is used to investigate the frequency fluctuations within the nonlinearity. Finally, it is further developed for two mode mass sensing.

In Chapter 4, TLL is used for two-mode gold nanoparticle sensing and mass spectra is obtained with a nonlinear resonator for the first time in literature. Finally, Chapter 5 concludes and mentions possible future works. I would like to point out that the work done here is published in [14].

# Chapter 2

## Nanoelectromechanical Resonators and Mass Spectrometry Applications

### 2.1 Fabrication and Characterization of NEMS Resonators

Top down fabrication technique is used for the fabrication of the doubly clamped beam resonators. Stoichiometric LPCVD Nitride on Silicon Wafers purchased from University Wafer for the fabrication of the devices used in the experiments. Nitride stress provided by the wafer manufacturer is stated state as “Film stress:  $> 800\text{MPa}$  Tensile Stress”. Nitride layer is 100 nm thick on a 500 micron silicon base.

Fabrication step starts with  $10\text{mm} \times 10\text{mm}$  square wafer (Figure2.1a). 300 nm of bilayer PMMA 495 A4 and PMMA 950 A2 are spin coated on top of the wafer (Figure2.1b). Pattern for contact pads and the electrodes on the beam are patterned with E-beam Lithography. This process is performed in Sabanci University Nanotechnology Research and Application Center (SUNUM). After

E-beam Lithography, PMMA dissolves as in the Figure 2.1c. In the next step, 100nm Au layer is deposited by thermal evaporation (Figure 2.1d). The wafer is left in an Acetone solution for the lift-off process and PMMA is dissolved as in Figure 2.1e. Next, PMMA is coated (Figure 2.1f) for the second E-beam Lithography for the beam pattern (Figure 2.1g). 60 nm of Cu layer is deposited by using E-beam Evaporation technique (Figure 2.1h). Cu layer is used as a hard mask to protect the beam structure from following etching process. After a second overnight lift-off of PMMA layer (Figure 2.1i), anisotropic Silicon nitride etch is performed with Inductively Coupled Plasma (ICP) (Figure 2.1j). Nitride etching is followed by isotropic Silicon etching with ICP to suspend the beam structure as it is demonstrated in Figure 2.1k. In the final step (Figure 2.1l), Cu layer is removed by wet etching by leaving the sample in Aluminum etchant solution for approximately 15 minutes. More details in fabrication is provided in [15].

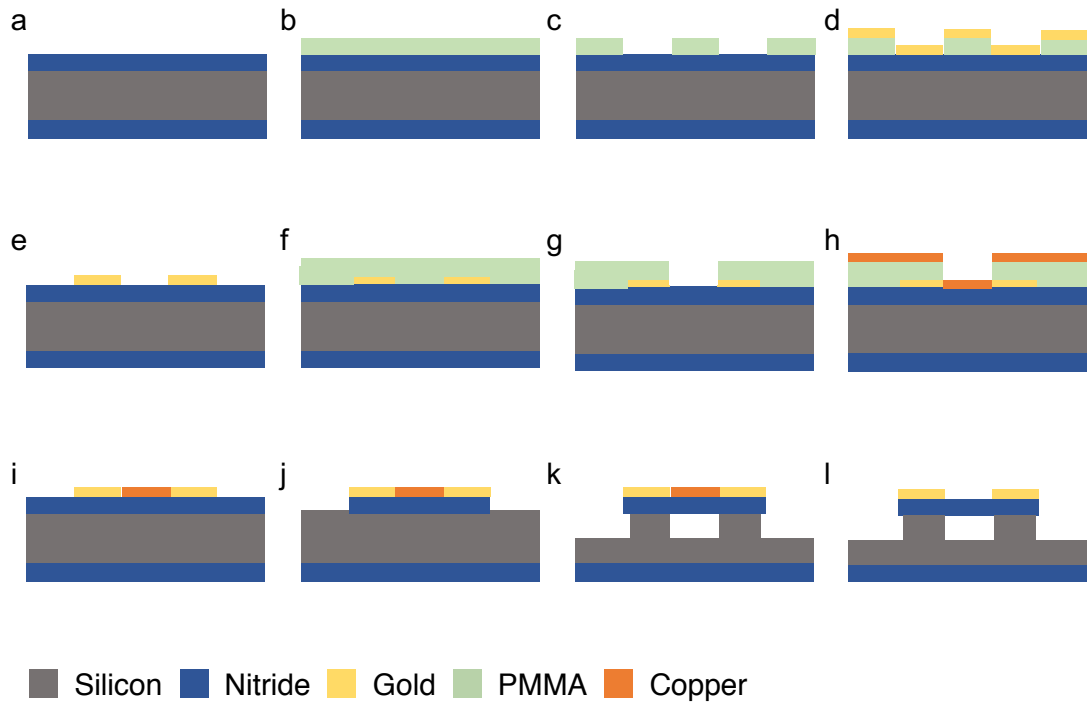


Figure 2.1: Fabrication steps of the doubly clamped beam nanomechanical resonators.

Scanning electron microscopy (SEM) images of the doubly clamped beam resonator after fabrication is demonstrated in Figure 2.2. After the fabrication, contact pads are wirebonded for ready to use.

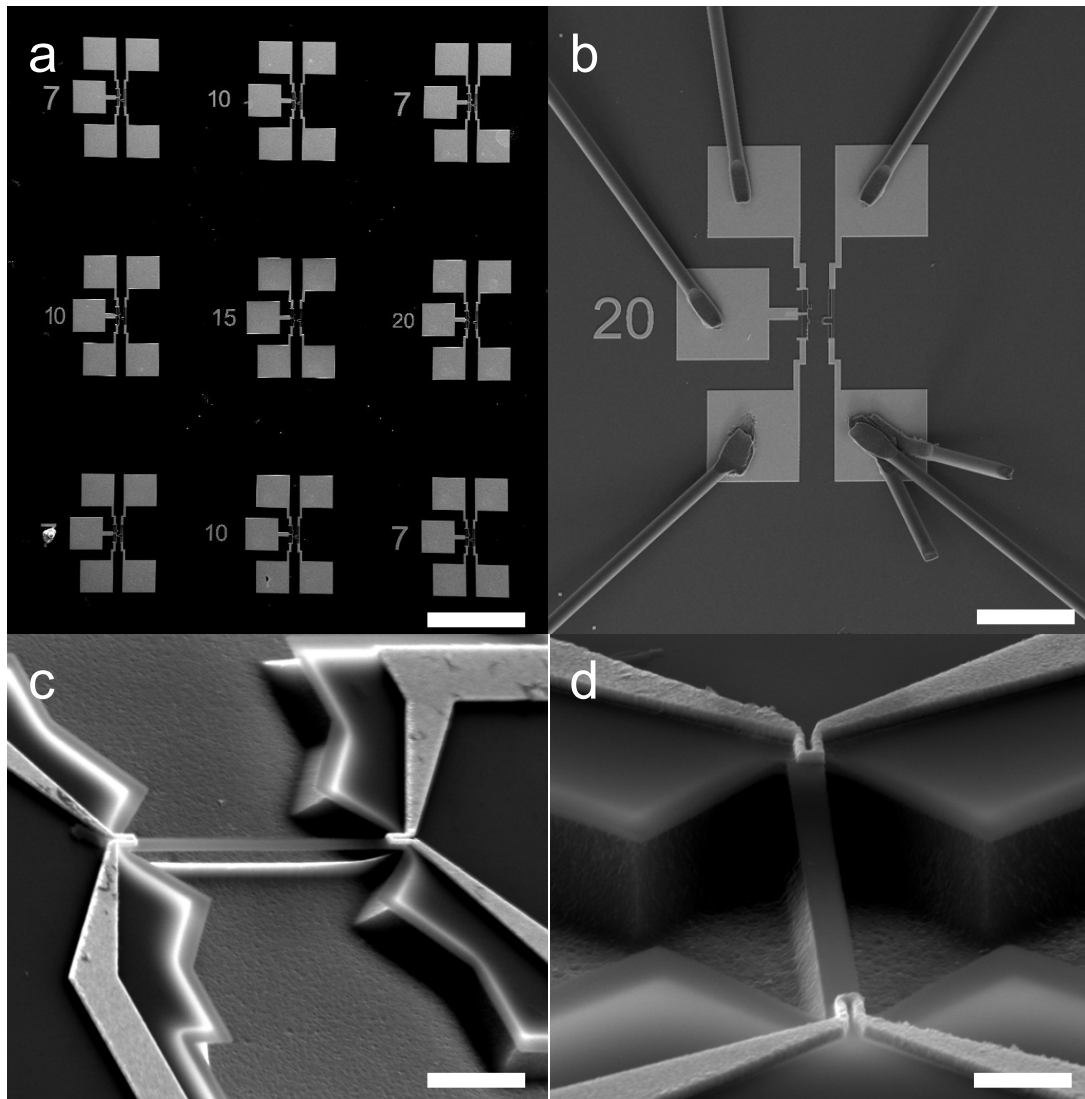


Figure 2.2: (a) In our design, one chip has 9 devices in variety of lengths. (b) 1 device has 5 contact pads that are used for actuation and detection of the resonance motion. (c,d) Bridge Silicon nitride resonator is demonstrated in different angles. Gold electrodes at the clamped ends are designed to reach less than %5 of the beam's total length not to disrupt the resonance mode shapes. White bar represents 300,100,5,2 micron respectively.

## 2.2 Motion in NEMS Resonators

A NEMS resonator vibrating in one of its resonance modes can simply be modeled as one-dimensional damped harmonic oscillator with a time-dependent drive force  $F(t)$ :

$$\ddot{x} + \frac{\omega_n}{Q}\dot{x} + \omega_n^2 x = F(t)$$

Here  $x(t)$  is the modal coordinate,  $\omega_n$  is the resonance frequency of the  $n^{th}$  mode, and  $Q$  is the quality factor (dissipation) in the resonator. Dissipation sources in the NEMS resonators has been investigated for many researchers and some of the sources include clamping losses, thermoelastic damping, and damping from surrounding fluids [1, 16]. Air damping is one of the well-known source of dissipation, therefore we use our resonators preferably in ultra high vacuum (UHV) environment (  $10^{-8}$  Torr). While the quality factor is found around 10 in the atmospheric pressure, in UHV environment it becomes 10000. The resonance frequency( $\omega_n$ ) is mostly determined by the geometry, material, and the stress on the structure.

Electromechanical transducers are used to convert the mechanical motion to electrical signal and vica versa. In this way, the motion in NEMS resonator can be actuated ( $F(t)$  can be adjusted) and also be detected. There is variety of available nanomechanical motion transducers for NEMS resonator [1]. In this work, we used thermoelastic actuation[17] and piezoresistive detection[18] methods for the operation of our resonator.

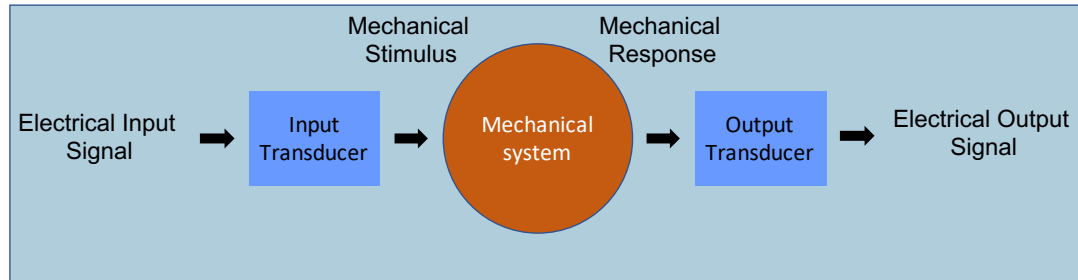


Figure 2.3: Transduction scheme of the NEMS resonator. Actuation and detection of the motion are obtained by the transducers which convert the mechanical motion to electrical signal and vica versa.

Thermoelastic actuation (Figure 2.4) is used to access higher order modes of the NEMS resonator. The principle of this actuation technique depends on the fact that different materials have different thermal expansion coefficient. In our case, these two different materials are the gold electrodes and the Silicon nitride beam. When a voltage ( $V$ ) is applied along the gold electrodes, it will create a localized Joule heating. In this process, stress will appear between two different materials due to different thermal expansions. As the heating is proportional to the  $V^2$ , the mechanical motion will take place at twice frequency of the frequency of the drive voltage [1].

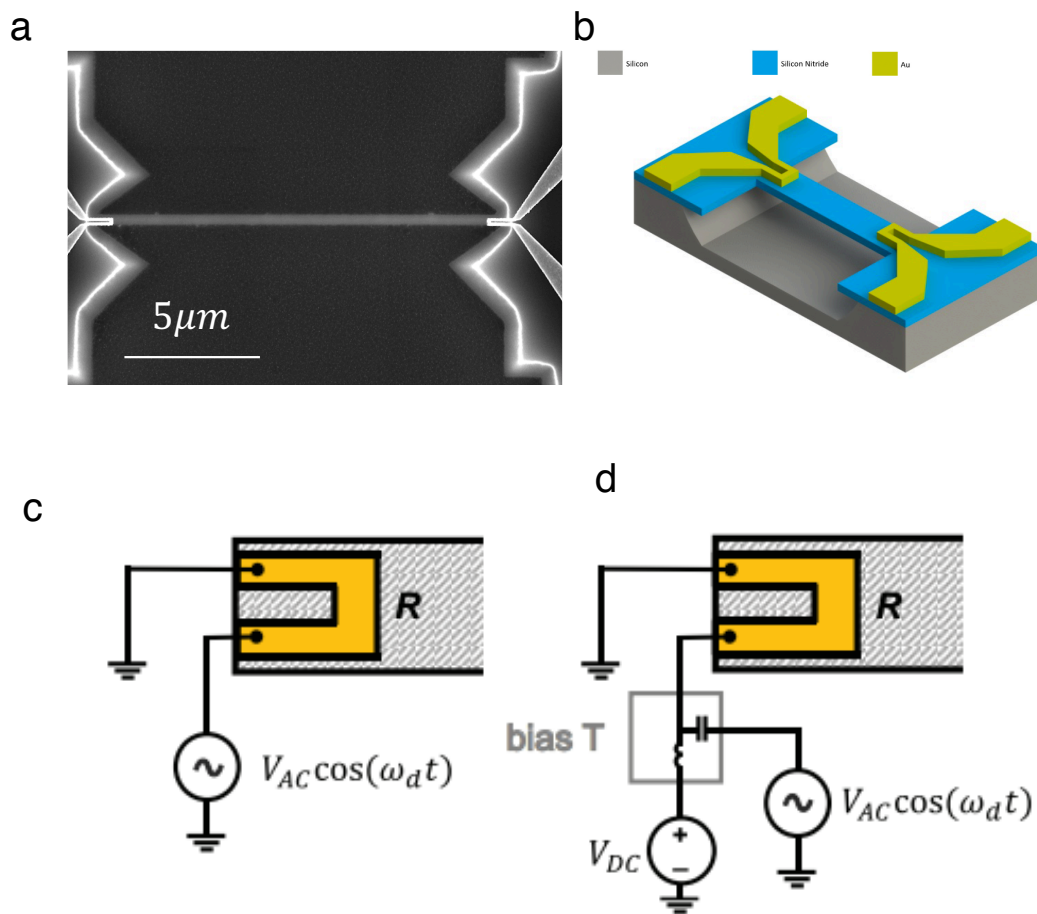


Figure 2.4: (a) SEM image of the doubly clamped beam resonator used for thermoelastic actuation and piezoresistive detection. (b) Materials are indicated for the resonator. (c,d) Thermoelastic actuation scheme with AC drive (a) and AC+DC drive(d). For the AC drive resonance condition is reached when  $\omega_{drive} = \frac{\omega_n}{2}$  and for the AC+DC drive; resonance is reached when  $\omega_{drive} = \omega_n$ . (c) and (d) are recreated from [1]

Piezoresistive effect is simply defined as the change of electrical resistance due to mechanical strain. Gauge factor ( $G$  - ratio of the change in resistance over the strain) of the piezoresistive material determines the sensitivity for the motion sensing. Overall, the relation between strain and the change in the resistance is given as;  $\frac{\Delta R}{R} = G\epsilon(t)$ . When the beam is vibrating at the frequency  $\omega$ , resistance

of the gold electrodes change also with  $\omega$  ( $R(\omega)$ ) due to the geometric effect induced by strain. Mathematically, the resistance can be written both with a constant and a dynamical term:  $R_{electrode} = R_0 + \Delta R \cos(\omega t)$ . There are two common ways to generate a voltage to readout the small resistance changes in the electrode. One way is to bias the resistance with a DC voltage and read the signal at  $\omega$  frequency. The other way is to apply a AC voltage of the form  $V_{bias} = V \cos((\omega + d\Delta\omega)t)$  and read the signal at  $\Delta\omega$  frequency [19].

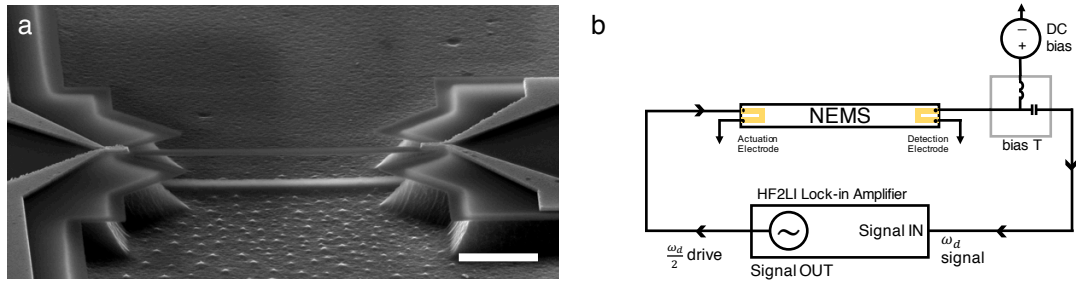


Figure 2.5: (a) SEM image of the 20  $\mu m$  doubly-clamped beam resonator used in the experiments. The scale bar is 5 micron. (b) Actuation and detection scheme implemented for the NEMS resonator are demonstrated. Simplicity of the electronic circuit allows feasible experimentation of the proposed method.

In Figure 2.5, we used direct readout with the DC bias voltage for the detection and actuated the motion with  $\omega_n/2$  drive signal. HF2LI Lock in amplifier allows us to produce the actuation signal at  $\omega_n/2$  and also detect the motion at  $\omega_n$ . In Figure 2.6, these actuation and detection schemes are used to obtain first resonance mode of the 20  $\mu m$  doubly clamped beam resonator.

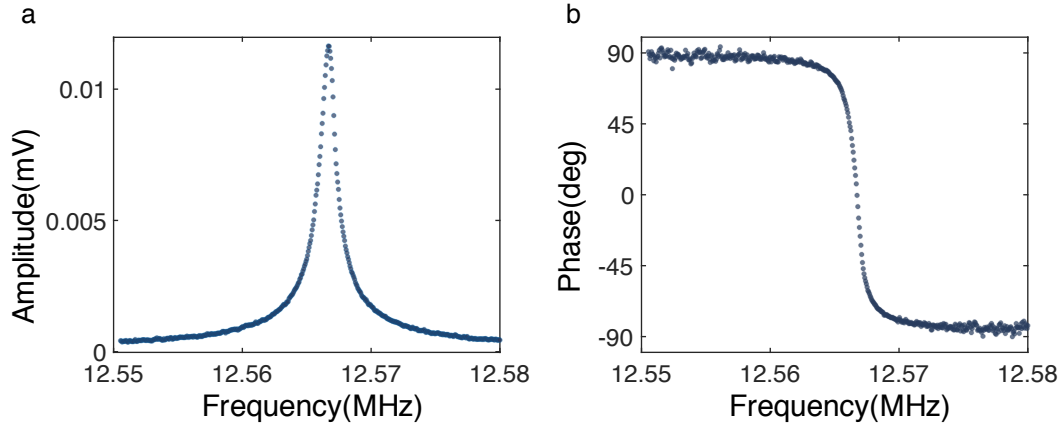


Figure 2.6: First resonance mode of the NEMS resonator obtained by thermoelastic actuation and piezoresistive detection methods. (a) Amplitude and (b) phase responses are measured with the HF2LI Lock in amplifier. Quality factor of the given mode is calculated as 12000 while the resonance frequency is at 12.567 MHz.

## 2.3 Motivation for Mass Sensing in Nonlinear Regime

Nanoelectromechanical Systems (NEMS) offer important advantages for mass sensing applications. In the last decade, the detection of single proteins [5], mass resolution at the atomic [20, 21] and near single-Dalton level [22], mass spectrometry at the single-protein level [6], and mass measurements of neutral species [8] have all been demonstrated. It was further shown that the information about the spatial distribution of analytes can be obtained by using multiple modes [11, 23]. More recently, the efficient transportation to and characterization of virus capsids by NEMS sensors [24] have been reported. These advances suggest that NEMS based mass spectrometry offers a competitive alternative to conventional mass spectrometry especially for analytes with molecular weight above the Mega-Dalton range.

Two aspects of NEMS devices are critical for high mass sensitivity: device miniaturization and the precise detection of the resonance frequency of the sensing structure. The former provides a strong scaling for the responsivity of the sensor [25] while the latter enables very small perturbations to be detected. However, certain limits are faced when optimizing both aspects. For example, if the device thickness is decreased to increase sensitivity — such as ultrathin NEMS [26, 27] and graphene/carbon nanotube devices [22, 28, 29, 30, 31]— the linear regime of operation shrinks for out-of-plane modes [2] (Figure 2.7. To preserve a large linear range, the length of the device may be scaled down as well: however, this approach comes with severe downsides such as a decrease in the capture cross-section of analytes and transduction efficiency, as well as, an increase in resonance frequencies which increases the parasitic background effects. For certain geometries and systems [2, 32] even thermal fluctuations are sufficient to drive the resonator into the nonlinear regime. This decrease in the dynamic range prohibits the use of such device architectures since the common practice in the field has been to keep the devices on resonance at the linear regime. To alleviate this limitation, many studies have sought to increase the linear dynamic range by suppressing nonlinearity [31, 33, 34, 35]. On the frequency detection aspect, the trend in the field has been to increase the drive power to decrease frequency noise and thereby increase the mass resolution. Although amplitude noise gets converted to phase noise in the nonlinear regime and environmental-induced frequency fluctuations increase with the increasing drive levels [36], sensing in the nonlinear regime provides additional handles on the system. For instance, by fine tuning the feedback parameters, reducing the total phase noise of the sensor (with respect to the oscillator with linear resonator case) is still possible [37, 38]. Moreover, as smaller sensors generate smaller signals generally, the ability to operate beyond the linear regime becomes critical to obtain a decent Signal-to-Noise Ratio (SNR). For these reasons, operation at the nonlinear regime holds great promise for sensing applications.

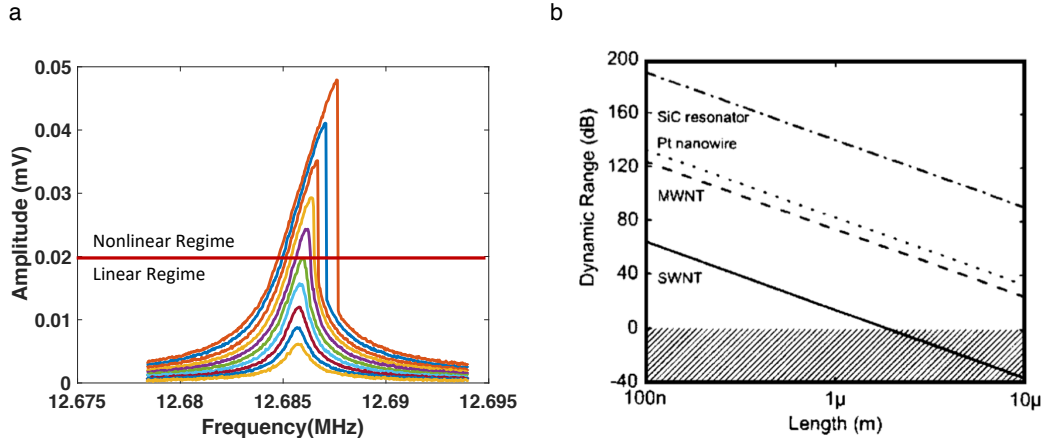


Figure 2.7: (a) Nonlinear regime provides better signal and wider operational range for NEMS resonators. (b) Linear dynamic range for several doubly clamped beam resonators. The shaded region indicates the absence of a linear regime. Figure is recreated from [2].

While the autonomous oscillator architecture offers excellent controllability [38, 39, 40], it is not always possible to build an oscillator circuit with nanomechanical devices since the signal-to-background ratio is usually small especially for smaller devices — making it difficult to satisfy Barkhausen condition only at the mechanical resonance frequency. On the other hand, a nanomechanical resonator can be readily driven by a frequency generator: indeed, this architecture is employed commonly in the form of open-loop frequency sweep or closed-loop frequency-tracking systems such as Phase-locked loops (PLLs). Many of the work in the past used the open-loop response of nonlinear resonators [41, 42, 43, 44], including a recent technique for accurate characterization of frequency fluctuations in the nonlinear regime [45]. However, continuously sweeping the frequency in the open-loop cannot be applied effectively to the sensing of abrupt changes induced by single analytes for two reasons. First, open-loop technique requires judicious re-setting of the sweep parameters every time after a particle adsorption. Second, each frequency sweep needs to comprise many data points for sufficient precision which implies long sweep times: as such, the effective frequency noise increases due to long-term drift effects. Another sweep based technique [44] has utilized

an extended frequency span and fast sweep parameters to calculate the particle-induced frequency shifts from the change in the amplitude response; however, since this technique is not adaptive, the accumulation of analytes would eventually shift the device parameters outside the sweep region. At the MEMS scale, the bifurcation sweep techniques near the amplitude jumps are reported [46, 47] and the detection sensitivity in the nonlinear regime is shown to be advantageous over the linear regime for mass detection of gas molecules [48]. Essentially, the techniques developed so far have not been designed to track the frequency at the nonlinear bifurcation point in an adaptive, closed-loop manner and have not been used in single entity (nanoparticle/molecule) sensing.

Apart from the aforementioned issues in the closed-loop implementations, the sensing applications of nonlinear resonators have so far focused on chemical sensing in the gas phase [43, 48, 49, 50]. Here, we have performed mass and position sensing of single nanoparticles with the first two resonance modes by developing a robust technique to track the resonance frequencies in the nonlinear regime. We have achieved  $10^{-6}$  Allan Deviation at about 1 second response time and collected about 500 single nanoparticle events and obtained the mass spectra of a 20 nm gold nanoparticle sample.

## Chapter 3

# A Method for Nonlinear Sensing: Trajectory Locked Loop (TLL)

The main ineffectiveness for the frequency tracking in the nonlinear regime comes from the lack of a powerful and robust method like phase locked loop (PLL) that is used for linear resonators. Although PLLs can conveniently track resonance frequency in the linear regime, the sharp phase transition and bistable response of nonlinear resonators (Figure 3.1c,d) prevent locking to a single phase at the resonance. Therefore, the nonlinear regime is generally avoided for mass sensing applications especially since performing a PLL does not look feasible in this regime.

In this chapter, we introduce a robust technique to track the resonance frequencies in the nonlinear regime, explain its working principle, and demonstrate the method for two-mode sensing with nonlinear NEMS resonators.

### 3.1 Introducing TLL

The device we used in the experiments is a  $20\ \mu\text{m}$  long,  $320\ \text{nm}$  wide, and  $100\ \text{nm}$  thick stoichiometric SiN device (with film stress of  $800\ \text{MPa}$ ) reported earlier[15]. In its linear regime, the phase response shows a sharp yet smooth transition (Figure 3.1b) which can be used as the reference target of a PLL circuit. When it is driven to the nonlinear regime though, it behaves as a Duffing resonator with stiffening nonlinearity[13] and hysteresis emerges as two different branches are observed depending on the sweep direction. The equation of motion becomes:

$$\ddot{x} + \frac{\omega_n}{Q}\dot{x} + \omega_n^2 x + \beta x^3 = F(t)$$

In our case, the Duffing nonlinearity ( $\beta x^3$ ) has a positive Duffing parameter ( $\beta$ ) meaning that nonlinearity assists the linear restoring force and makes the resonator stiffer. Therefore, it is called stiffening nonlinearity. More importantly, two sharp transitions (with theoretically infinite slope) in the amplitude (Figure 3.1c) and phase (Figure 3.1d) are observed. The transition at the higher frequency is denoted as  $f_{up}$  when sweeping from left to right and the one at the lower frequency is denoted as  $f_{down}$  when sweeping from right to left. As shown before[45], these transition frequencies are related to the resonance frequency and effective mass of the structure. Therefore, continuously tracking either of these frequencies can be used to detect single particles landing on the structure. However, an architecture based on sweeping the frequency with an open loop configuration results in a slow response time and the corresponding Allan Deviation degrades due to long-term drift effects. On the other hand, building a feedback loop is very challenging due to the infinite slope at these transition frequencies.

To overcome this problem, we aimed to keep the sensor trapped inside the hysteresis window of the phase response (Figure 3.1d) rather than locking to a single phase. Boundaries of the hysteresis window are defined as the points where the sharp frequency jumps ( $f_{up}$  and  $f_{down}$ ) occur. At the upper boundary, phase jumps from point C to D on the curve in Figure 3.1d, and at the lower boundary phase jumps from point A to B. Therefore, any controller which tries

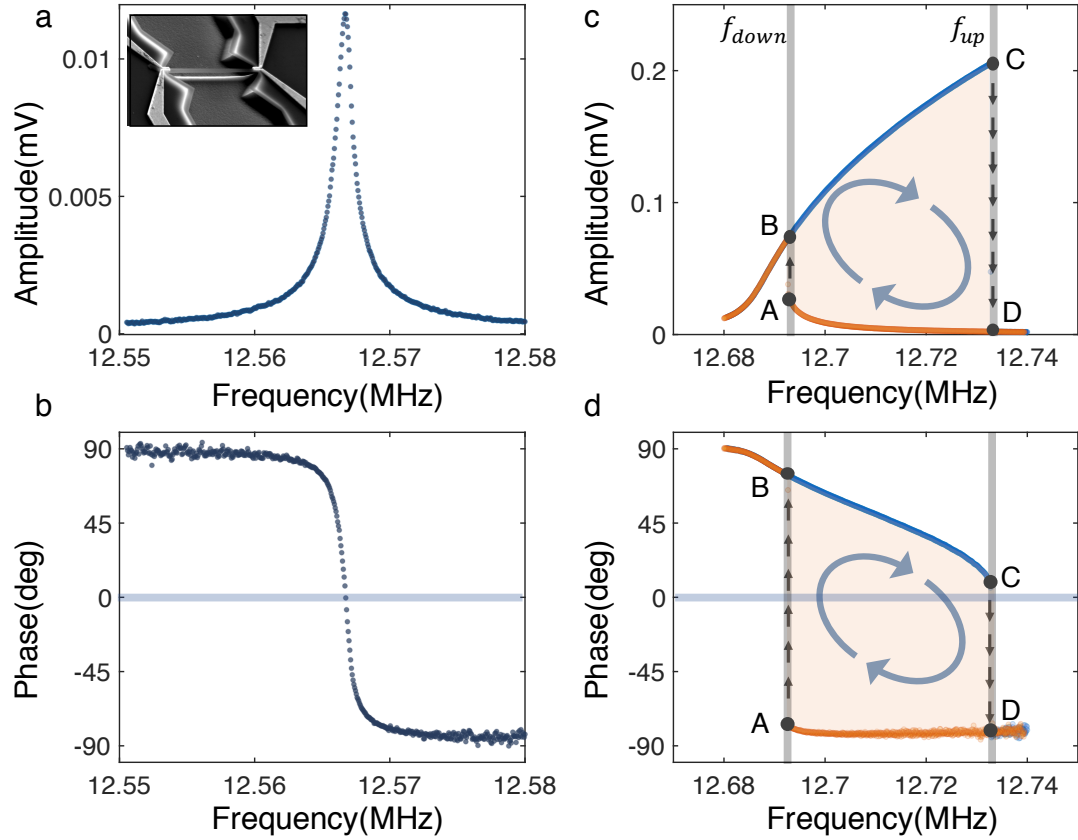


Figure 3.1: Linear and nonlinear response of the NEMS resonator (a,b) In the linear regime, a sharp phase transition is observed with the quality factor of 12000.  $0^\circ$  crossing in phase can be used as a reference target for PLL. The inset shows the SEM image of a typical doubly-clamped beam resonator used in the experiments. The scale bar is 3 micron. (c,d) The resonator acts as a ideal Duffing resonator with a positive Duffing term when it is driven with larger excitations. Nonlinear phase jumps are observed depending on the sweep direction (blue and orange data points for the sweep from left to right and from right to left respectively).  $f_{up}$  and  $f_{down}$  frequencies are defined at the boundaries of the hysteresis window. In the colored area, the resonator shows a bistable response.  $0^\circ$  phase cannot be locked with the PLL as it is in the unstable region of the nonlinear response.

to be locked to a target phase at the sensitive jump frequencies cannot succeed since noise would push the PLL out of the operation point. However, the jump frequencies can be used for keeping the system circulating inside the hysteresis window.

To understand the method, we consider the nonlinear resonator with the phase response given in Figure 3.1d. We assume that there is a feedback controller with the target phase at 0 degrees: none of the stable branches shown in Figure 3.1d contains this point: indeed, this point lies only on the unstable branch of the resonator (not shown in Figure 3.1c-d), hence it is not accessible within this measurement architecture. Therefore, the controller cannot keep the system locked at 0 degrees: however, a different dynamic emerges under these conditions. Whenever the phase has a positive value, the controller will increase the driving frequency; and whenever, the phase has a negative value, the controller will decrease the driving frequency. For this reason, starting from a random point, the controller will first push the system to the boundary of the window (i.e. until when the drive frequency is either  $f_{up}$  or  $f_{down}$ , depending on the initial condition). After passing through either of the jump frequencies ( $f_{up}$  or  $f_{down}$ ), the sign of the phase flips, therefore the controller action reverses automatically and the system now starts traversing the other branch in the opposite direction. In effect, the system continuously circulates within the hysteresis window (Figure 3.1d), automatically tracing the boundary defined by the two jump frequencies. Although the control system is similar to the PLL, no phase is locked in this system, therefore we cite the proposed method as a trajectory-locked loop (TLL) for the convenience.

TLL can be used to analyze frequency fluctuations of the nonlinear bifurcation points. During one cycle of TLL, it is possible to extract both the values of  $f_{up}$  and  $f_{down}$  by looking at the sign of the derivative of the frequency with respect to time (Figure 3.2a-b). As it is demonstrated in Figure 3.2b,  $f_{up}$  can be identified as the point where the derivative changes sign from positive to negative and vice versa for  $f_{down}$ . Figure 3.2c shows TLL operation in both phase and frequency domains. The phase response of the nonlinear resonator passes through a similar trajectory over time and keeps the system inside the hysteresis window as it can

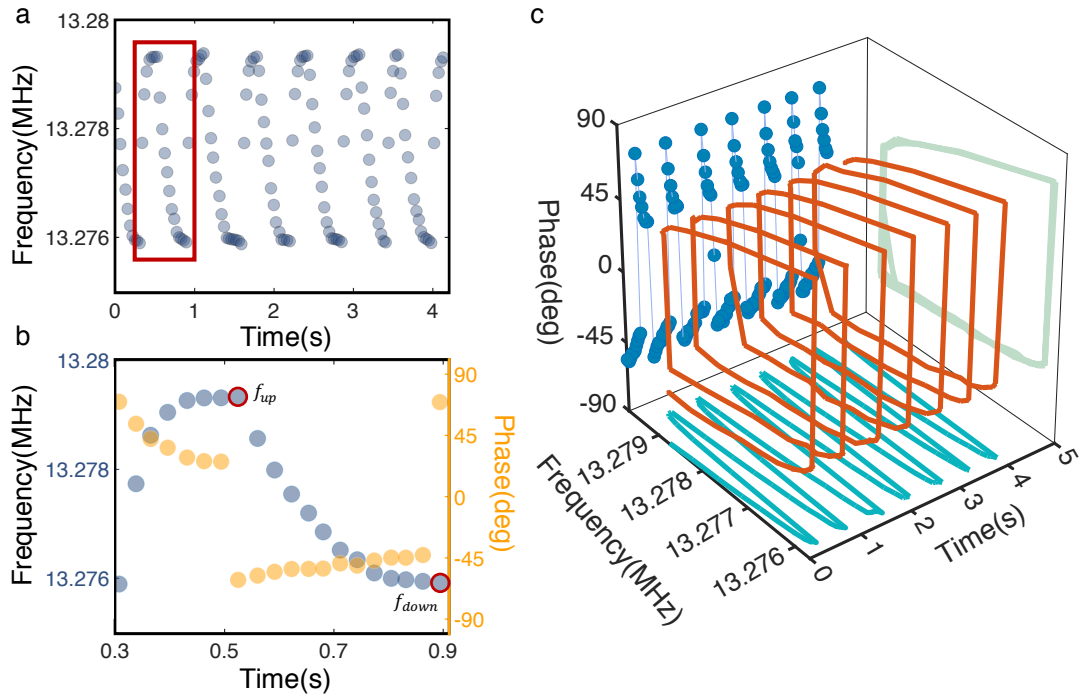


Figure 3.2: Trajectory Locked Loop (TLL). (a) The controller is adjusted for highly sensitive measurements of bifurcation frequencies. Circle data points show the frequency sweep steps which becomes denser while getting closer to the boundaries. (b) The one full cycle indicated with a red rectangle in (a) is maximized and plotted with the corresponding phase response. It is possible to extract  $f_{up}$  and  $f_{down}$  at the points where the phase jumps with a near infinite slope as they are indicated with red circles. For the given case, notice that one cycle approximately takes 0.6 seconds which can be comparable with many of the PLLs used in this field. (c) The projection of the TLL over time is displayed. It can be clearly seen that TLL holds the nonlinear resonator inside the hysteresis window.

be seen at the projection of the frequency-phase plane. Projection of the data onto the phase-time plane clearly illustrates the phase jumps at the boundaries of the bistable regime.

The speed and precision to estimate the frequencies at bifurcation points in one TLL cycle depend on the controller architecture. Although the feedback controller has the same purpose for TLL and PLL, as in both case controller tries to be locked to a single phase, the control dynamic is different since the phase error in TLL systems will always oscillate between high positive and negative values due to phase jumps. Therefore, extra cautions should be taken for the design of TLL controller. For example, the integration controller over phase error to determine the frequency step which will be added to former drive frequency is used to prevent offset in PLLs, it causes overshoots for capturing bifurcation points for TLLs. If we consider the lower bound of one TLL cycle where the phase is negative and the controller steers the frequency from right to left, the error will accumulate with the integration controller action (with respect to phase error) and just as the bifurcation point is passed, the accumulated error will still try to keep the same controller direction (whereas the direction should change). The same situation holds for the upper bound, consequently we found that the integrative controller, an essential part of PLLs, causes overshoots on the frequency measurements for TLLs. In order to increase the precision of the controller while detecting the bifurcation frequencies, we used the threshold phase values at the boundaries of the unstable regime (point C and point A in Figure 3.1d) for the error calculation. The controller is designed to adjust the frequency changes proportional to its distance from the boundaries of the hysteresis window, as evident in Figure 3.2b. In other words, when the phase of the resonator comes closer to one of the bifurcation thresholds, frequency steps between each sweep are decreased in order to reduce the offset error. Moreover, a larger step size while the resonator is away from the jump points increases the speed of the operation. In this way, accurate and fast measurements for  $f_{up}$  and  $f_{down}$  are achieved. In Figure 3.2a, these two frequencies are measured with an averaging time 600ms, which is sufficient short to avoid drift effects. The speed of the TLL can be adjusted for smaller integration times and we demonstrate TLL with 35ms loop

time in the following subsection as I also provide more details on TLL operation.

## 3.2 Controller Design

TLL controller is similar to feedback controllers that are used for PLL. The main difference is the change in the control dynamics as the phase error will always exist and oscillate between much higher errors than in phase-locked systems. Therefore, the feedback controller has to be adjusted by considering the nonlinear response of the resonator.

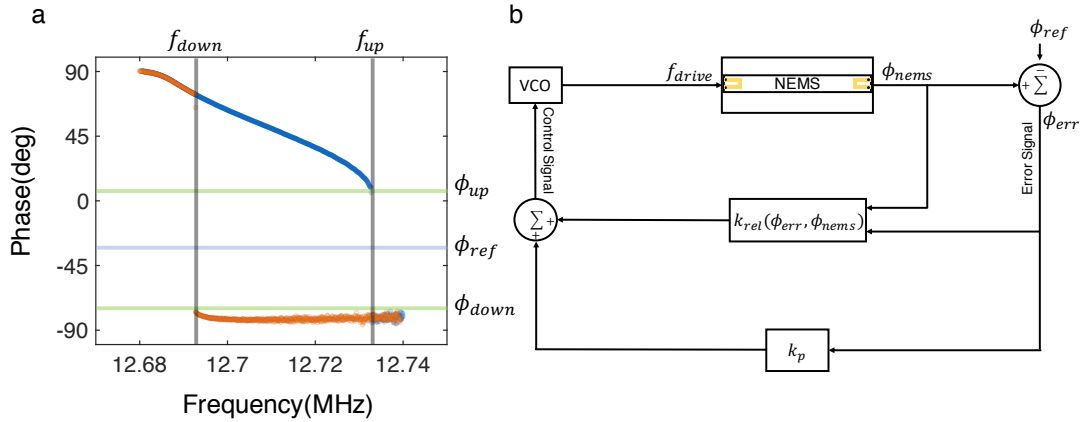


Figure 3.3: (a) Nonlinear phase response of the resonator is demonstrated with the boundaries of the bistable regime.  $\phi_{up}$  is the phase value right before the jump takes place while sweeping from left to right and vice versa for  $\phi_{down}$ . (b) Controller design for the TLL.  $\phi_{up}$  and  $\phi_{down}$  are used to adjust the total gain in the system: gain is decreased when the phase response of the resonator is getting closer to one of the thresholds, therefore frequency steps are also reduced for more accurate measurement of the  $f_{up}$  and  $f_{down}$ . NCO stands for Numerically Controlled Oscillator.

The first step for the feedback controller of TLL is the determination of the reference phase. As it is demonstrated in Figure 3.3a, any phase between the two

jump points ( $\phi_{up}$  and  $\phi_{down}$ ) is in the unstable region of the nonlinear resonator, which cannot be observed experimentally, therefore can be used as a reference phase ( $\phi_{ref}$ ) for trajectory locking. In our case, the reference phase is chosen at the same distance from both threshold phases ( $\phi_{ref} - \phi_{down} = \phi_{up} - \phi_{ref}$ ). Note that one can adjust the reference phase to zero degrees by shifting the entire phase response to simplify the error calculations.

The second step is to write the algorithm for the feedback controller which will be used for the precise and fast measurements of the jump frequencies. Frequency step size is adjusted via the controller design, therefore precision and speed will depend on the controller's skills. In our case, we adjusted our controller in a way that frequency steps are bigger when the phase of the resonator is far from jump phases and smaller when it is close to the jump points. Depending on the sign of the phase error ( $\phi_{err} = \phi_{nems} - \phi_{ref}$ ), it is possible to determine the state of the resonator on the hysteresis window (upper branch if the error is positive, lower branch if negative). In our feedback algorithm, the sign of the phase error is used to calculate the relative gain ( $k_{rel}$ ) which adjusts the frequency steps for accurate measurement of the frequencies at the bifurcation points (Figure 3.3a).  $k_{rel}$  is defined as;

$$k_{rel}(\phi_{err}, \phi_{nems}) = \left\{ \begin{array}{ll} \text{if } \phi_{error} > 0 & (\phi_{nems} - \phi_{up})k_{up} \\ \text{otherwise} & (\phi_{nems} - \phi_{down})k_{down} \end{array} \right\}.$$

Proportional gain ( $k_p$ ) is also implemented to the controller architecture for the continuous sweep operation. For example, when the phase response of the resonator is equal to the bifurcation phase at the upper branch ( $\phi_{nems} = \phi_{up}$ ), phase error will sweep the resonator while relative gain will be equal to zero. At the end frequency step is calculated in the following way;  $f_{step} = (k_{rel} + k_p)(\phi_{err})$ .

From this algorithm, we can observe that  $k_{rel}$  plays an important role in adjusting frequency steps as it decreases while approaching one of the jump points (Figure 3.3). Also, the algorithm we used here is just one example of the many other practicable control algorithms, therefore we would like to point out that

the same TLL operation can be achieved with different controllers.

The speed of the one cycle inside the TLL is determined by how fast the frequency is swept between two jump points. As we increase the drive strength, nonlinearity will be more pronounced and eventually, the distance between the jump points will be widened. Therefore, while determining the control parameters, we take the frequency range of the hysteresis window (the region between  $f_{up}$  and  $f_{down}$ ) into account.

The speed of sweep operation depends on the frequency step size and the instrument's speed (in our case, HF2LI Lockin controlled via MATLAB API, so there is also a communication time between computer and the instrument). Frequency step size is adjusted via the controller design, therefore the speed will mostly depend on the controller's skills. Feedback controllers for PLL systems are widely used and very well developed in the industry and in some cases, PLL controller is embedded in the hardware (e.g. HF2LI-PLL option) resulting in faster frequency tracking since it eliminates the communication between hardware and software. As feedback controller for TLL is developed as a form of the PLL controller, these fast PLL systems can also be used for fast TLL operation with the wise selection of the PID parameters. In Figure 3.4, we demonstrate the TLL operation performed with HF2LI-PLL option and in this case one loop completed in 35 ms. Moreover, the frequency shifts due to gold nanoparticles captured by the TLL with 100ms loop time are demonstrated in Figure 3.4.

Substantially, it is easy to adjust TLL's speed and precision with simple feedback control algorithms. In our case, we designed our feedback controller according to our device and experimental conditions and adjusted the precision and speed of the TLL for better mass resolution.

The resolution of the nonlinear sensing technique depends on the TLL's precision of measuring the jump frequencies and the frequency fluctuations of the jump frequencies. For the precision of TLL, since we know the phase value at the frequency jump, feedback controller reduces its frequency step size while approaching one of the jump phases. For example, in the Figure 3.5, we zoom into

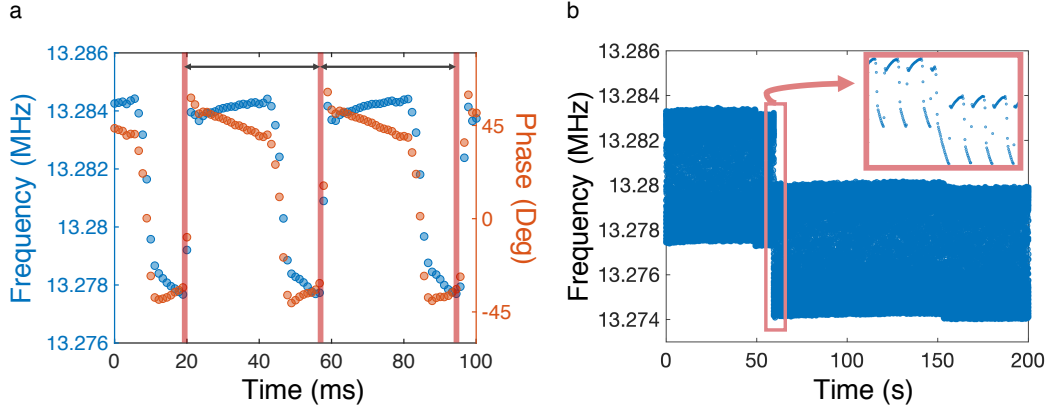


Figure 3.4: (a) TLL performed with 35ms loop time. Red lines indicate the recorded  $f_{down}$  points and the black arrows are used to indicate the same time interval between 2 measurements. (b) Frequency shifts due to gold nanoparticles are captured with the fast TLL time (100ms).

one cycle of TLL (Figure 3.2b) in order to show the precision of TLL while measuring  $f_{up}$ . In this case, we can observe that TLL controller reduces the frequency step down to 4 Hz just before the phase jump. Now, knowing that actual  $f_{up}$  is some value between these two frequencies (13279315 Hz and 13279319 Hz) separated with 4 Hz, we can extract  $f_{up}$  from this information. One way to extract  $f_{up}$  is to take the frequency data where the phase jump occurred ( $f_{up} = 13279319$ ) or take the average of these two frequencies and calculate  $f_{up} = 13279317 \pm 2$  Hz. Either technique can be used since the measurement has error less than % 0.00003.

When we increase the drive strength, nonlinearity will be more pronounced and eventually the hysteresis window will be widened. However, this can only affect the speed of the TLL cycles rather than its precision for measuring the jump frequencies, because although the hysteresis window is widened, phase response will be similar and controller will do the same action by reducing the frequency step size when the phase response is closer to one of the jump phases. Also, when the hysteresis window widens, controller parameters can be adjusted to prevent the redundant time for covering the large hysteresis range while making

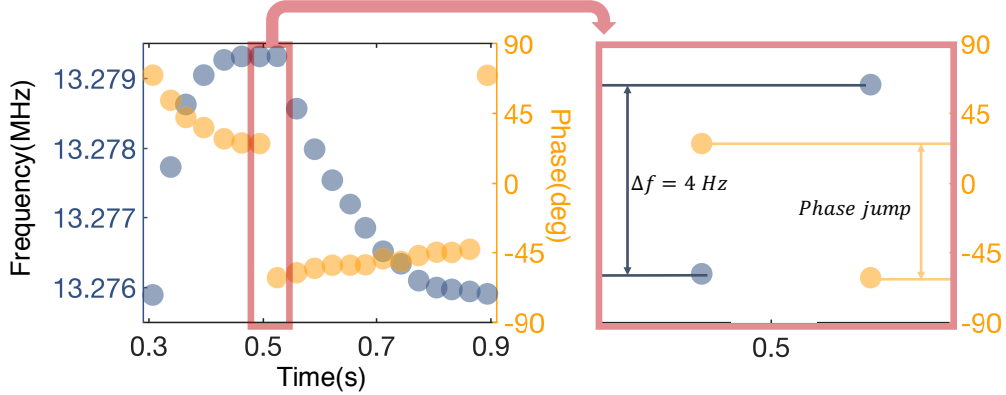


Figure 3.5: (a) One TLL cycle inside the hysteresis window, as it is also used in Figure 3.2b in the main text. (b) Red rectangle in (a) is zoomed for better realization of the small frequency step (4 Hz) just before phase jump.

no compromises from the precision of the measurement. For example, one way to deal with this could be to define a new proportional gain constant relative to some phase value ( $\phi'_{up}$ ) which is bigger than the phase at the jump point. For example, let us consider  $\phi_{up} = 43$  and the hysteresis window is 20kHz wide so that when  $\phi_{nems} = 90$ , TLL has to cover 20 kHz range to reach to the upper jump point. We can pick  $\phi'_{up} = 50$  and then write our algorithm to sweep the frequency with larger step size till phase response reaches 50 degrees, and then slow down till jump takes place. Possible algorithm would be:

$$f_{step} = k_{up}(\phi_{nems} - \phi_{up}) + k'_{up}(\phi_{nems} - \phi'_{up}) + k_p(\phi_{nems} - \phi_{ref}) .$$

Therefore, for the controller design we take the frequency range of the hysteresis window (the region between  $f_{up}$  and  $f_{down}$ ) into account as we are mainly interested in rapid and precise measurements of the jump frequencies.

Although TLL can easily be adjusted for precise and fast measurements of jump frequencies, the resolution of nonlinear sensing deteriorates with increasing drive strength due to increasing frequency fluctuations in the resonator. As Maillet et al. observed a similar effect with the nonlinear resonators for longer

time averaging of the jump frequencies, we explained our similar observations for shorter integration times and we applied the method for mass sensing.

Using one of our devices we tested how TLL would behave with small signal to background ratio (SBR) where the background is high. To simulate the background effect, we added a signal at  $\omega$  frequency to the drive signal ( $\frac{\omega}{2}$ ). As the mechanical motion is at  $\omega$  and so as the detection, insertion of other signal at  $\omega$  increases our background. In Figure 3.6, we compare three different cases: (a) no additional background is introduced to the system, signal (calculated from the max amplitude of  $f_{up}$ ) to background ratio is approximately 30, (b) SBR is reduced to 2 by increasing the background, (c) SBR is reduced to 1. In all these 3 cases, we demonstrate the amplitude and phase responses of the resonator, and at the bottom we show the TLL data. As the reviewer also points out, in the case of a large background the phase jump is much smaller than the case with no background. However, we observe that phase jump may be reduced but the sharp transition still remains and the sharp phase transition is enough to perform TLL operation. Controller can require an adjustment to increase the speed of the TLL as the error will be smaller with the small phase transition, however, this is just the change of the control parameters as the essential idea remains same. Moreover, large background will also reduce the phase transition and SBR for the linear regime which will also affect the PLL operation. In this case, increasing the signal with nonlinear motion would be more useful to operate.

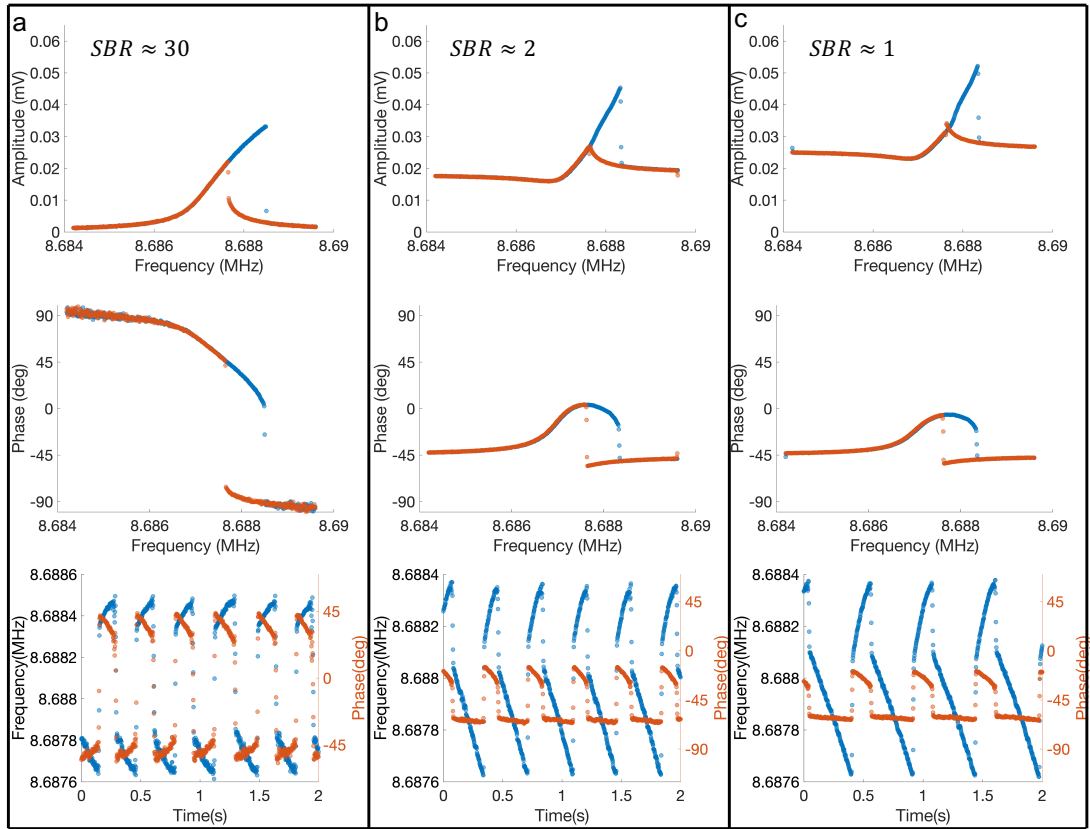


Figure 3.6: Amplitude response, phase response and TLL operation are demonstrated from top to bottom for three different SBR.

In conclusion, TLL is a convenient and practical method to track bifurcation frequencies at nonlinear regime. TLL is fast as it can capture both bifurcation frequencies with 35 *ms* loop time while the other open loop configurations [45] result in more time (10 *s*) to capture a single bifurcation frequency. Close loop controller architecture of TLL can be adjusted for fast and precise measurements of the bifurcation frequencies which can be used for analyzing the frequency fluctuations and mass sensing in nonlinear regime.

### 3.3 Frequency Fluctuations in Nonlinear Regime

After showing that TLL can track the bifurcation frequencies, we further used it to characterize the frequency fluctuations of the first two modes by calculating Allan deviations in the nonlinear regime. The ability to operate in nonlinear regime provides a wide-range of drive powers to be applied for the actuation of the resonator. Therefore, we calculated Allan deviations of the first two modes at different power levels in order to find the appropriate drive for the mass-position sensing of 20 nm gold nanoparticles.

Frequency fluctuations are measured in nonlinear regime with TLL to confirm its utility for the mass sensing and the Allan deviations are compared with the measurements from linear regime with PLL. For the calculation of the Allan deviations of jump frequencies with TLL, the jump frequencies are extracted from each cycle of TLL, as it is demonstrated in Figure 3.2. By keeping the time trace of these points (Figure 3.7), we calculated the Allan deviations for each mode (Figures 3.8 and Figure 3.9). As each loop is completed within the same time interval (with tolerable measurement error), this allows us to analyze the frequency fluctuations with different integration times.

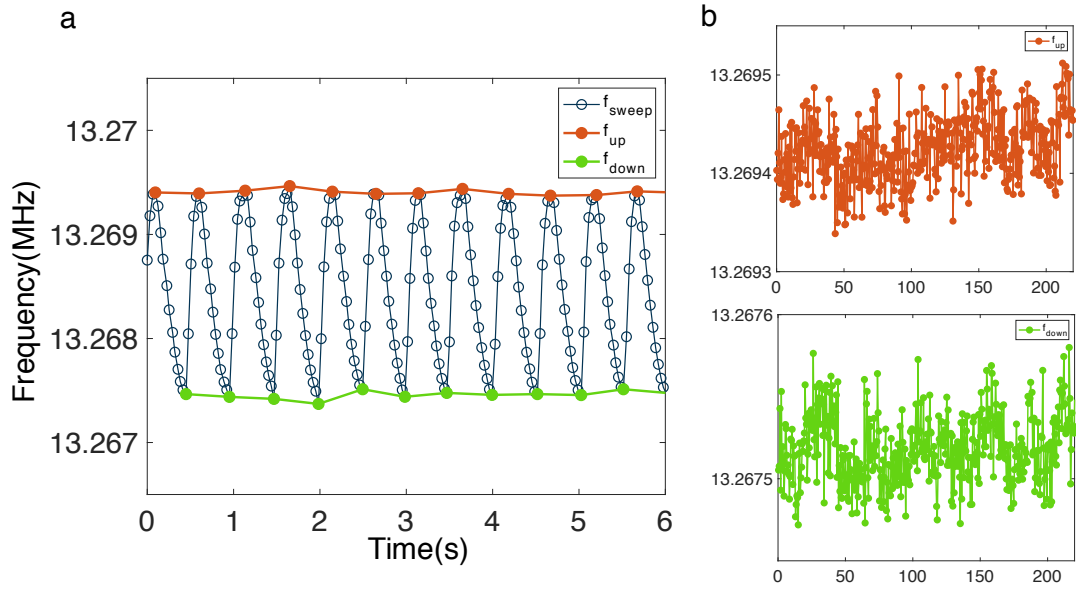


Figure 3.7: (a) Jump frequencies ( $f_{up}$  and  $f_{down}$ ) are extracted from TLL operation. (b) Time trace is captured with the frequency and then later used for Allan deviation calculation.

The procedure is performed for the first two modes of the resonator and repeated with the different drive voltages (Figure 3.8 and Figure 3.9). The results demonstrate that the fluctuations at the lower bifurcation point ( $f_{down}$ ) promises favorable conditions for mass sensing comparable to the fluctuations at the linear regime.

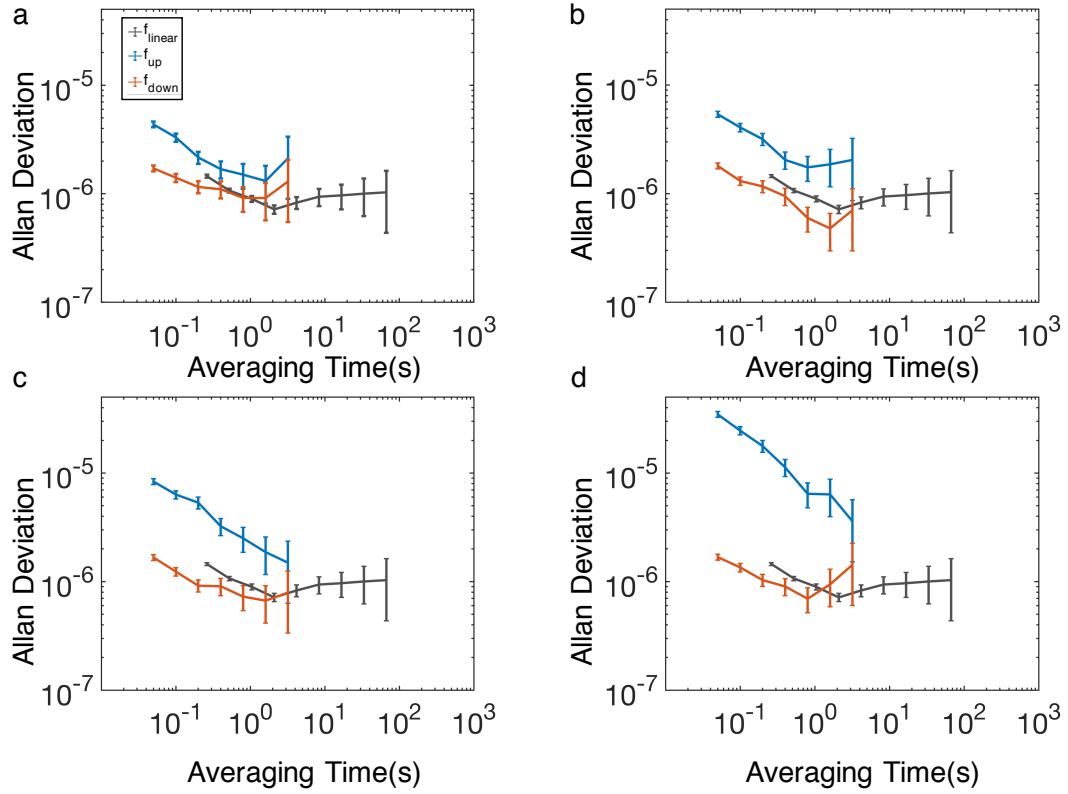


Figure 3.8: Frequency instabilities for the first mode frequency in nonlinear regime is investigated at different drive powers. The actuation voltage is increased from (a) to (d). Allan deviations at the linear regime (dark grey line) are compared with fluctuations at  $f_{\text{up}}$  (blue line) and  $f_{\text{down}}$  (orange line). The nonlinear drive voltage levels for a-d are: 75, 85, 95, 115mV respectively (half-omega drive is used). We note that the cycle time of the TLL was 1 seconds; however, noise statistics should be reported starting from 50ms averaging time scale as it is the duration between each point within the cycle. With 50ms duration between each point, the first data on the Allan deviation plot occurs for a 50ms averaging time and a 950ms dead time. Owing to the overall white FM characteristics, the dead time does not play a significant role.

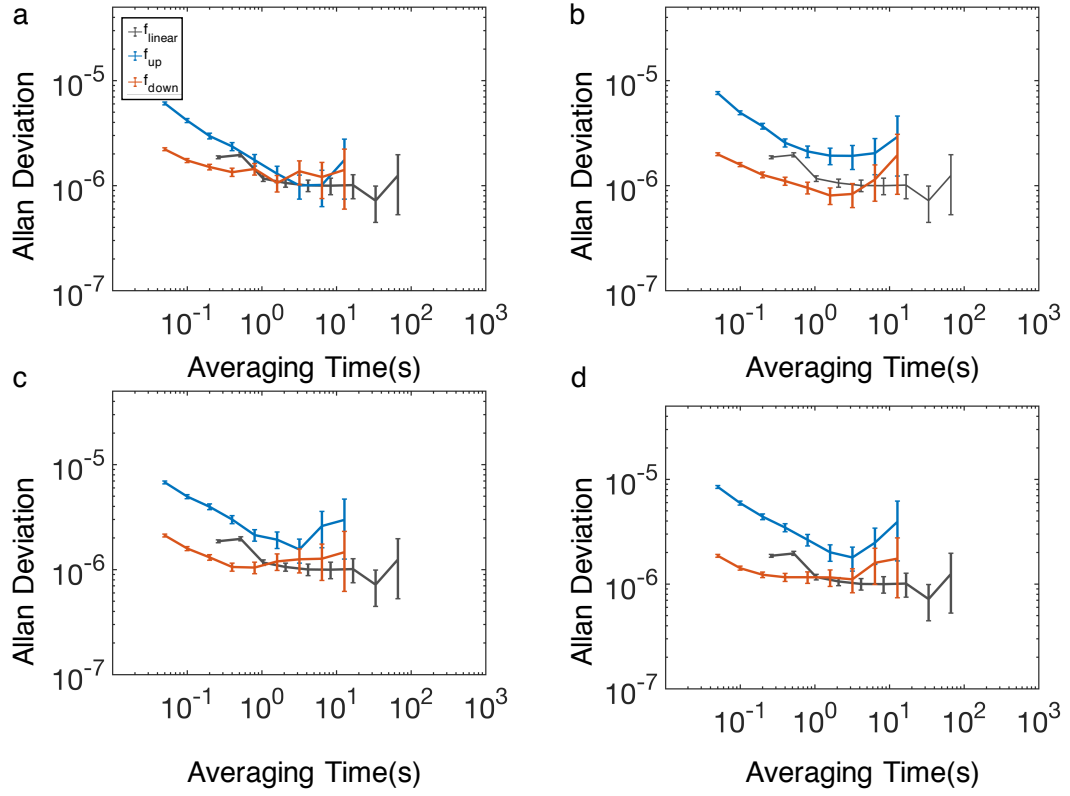


Figure 3.9: Frequency instabilities for the second mode frequency in nonlinear regime is investigated with the same method mentioned in Figure 3.8. The nonlinear drive power levels for a-d are : 112.5, 122.5, 125, 140 mV respectively (half-omega drive is used).

### 3.4 Sequential TLL for Two Mode Sensing

As we want to use the nonlinear resonators for single nanoparticle detection, we need to measure the analyte-induced frequency shifts of the first two modes [6, 51, 52]. However, exciting the two modes simultaneously poses a challenge, since intermodal coupling [15, 53, 54, 55, 56], which may interfere with analyte-induced frequency changes, becomes more pronounced as the mode amplitudes reach nonlinear regime. Thus, extra care is needed for two-mode sensing with nonlinear resonators. To minimize the interference of coupling effects between the modes, we use TLL sequentially as it is demonstrated in Figure 3.10. In this method, as one full-cycle is completed inside the hysteresis window for the first mode (meaning that  $f_{1_{up}}$  and  $f_{1_{down}}$  are detected), another cycle starts for the second mode (so that  $f_{2_{up}}$  and  $f_{2_{down}}$  are detected next). We note that, to avoid time delays due to power switching between modes during the sequential TLL operation, the inactive mode continues to be driven at the constant frequency which is close to the end frequency of its previous TLL cycle. As the cycle finishes at the lower bound, the inactive mode stays on the low-amplitude branch while the active mode circulates inside its TLL cycle. Thus, the effect of the intermodal coupling on the measurements is minimized.

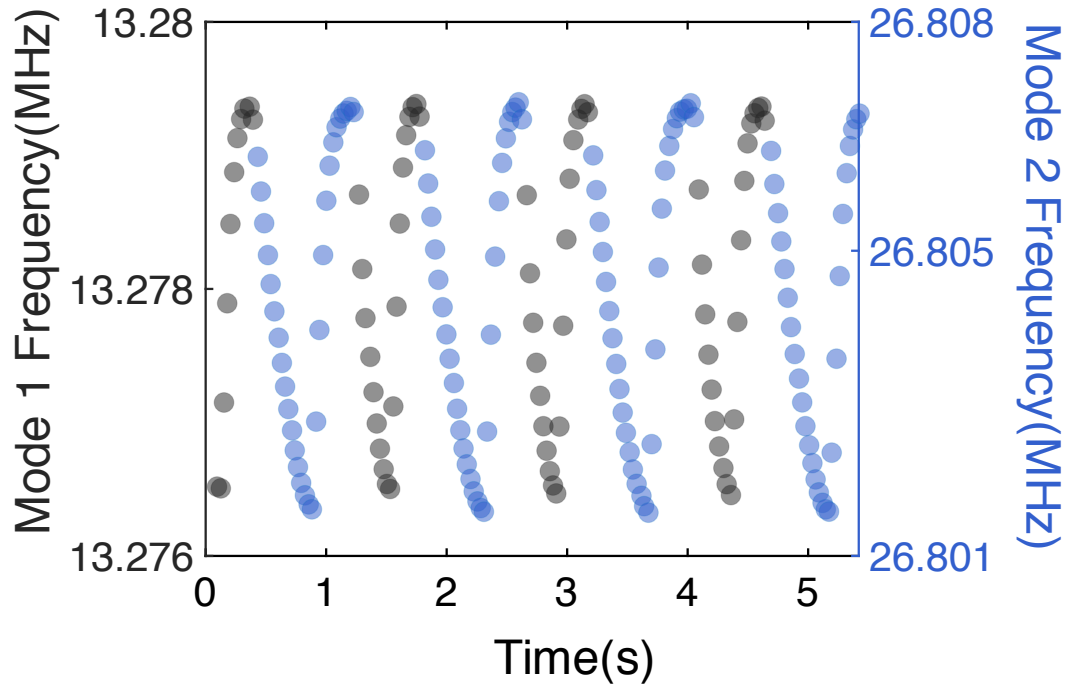


Figure 3.10: First and second resonance modes are tracked by TLL sequentially in order to minimize coupling between two nonlinear modes. After one mode completes the one full cycle inside the hysteresis window, the other mode is driven by TLL.

# Chapter 4

## Single Nanoparticle Sensing in Nonlinear Regime

### 4.1 Experimental Setup

We used thermoelastic actuation [17] and piezoresistive detection [25] techniques for the dynamic characterization of the doubly clamped SiN beam resonator as they are explained in Chapter 2. Fabrication process of the resonator is also explained in Chapter 2. HF2LI Lock-in amplifier is employed to the experimental setup for generating the actuation voltage and reading the detection signal by internal referencing. Matlab is used as a programming interface for the control of the lock-in amplifier which then configured to implement controller for PLL and TLL. Matlab codes are also provided in the Appendix.

The resonator is placed inside the vacuum chamber (Kurt Lesker) which is pumped down the pressure approximately  $1 \times 10^{-8}$  Torr. All the experiments are conducted at room temperature (24°C). For the molecule delivery, Matrix Assisted Laser Desorption/Ionization (MALDI) is used. In this method, the target with the matrix compound is bombarded with the laser source which excites the spot with energy. As a result of this, desorption occurs and molecules fly

throughout the target area [57].

For the MALDI system of the 20 nm diameter gold nanoparticles, similar technique is used with the earlier work [21]. Experimental setup is demonstrated in Figure 4.1.

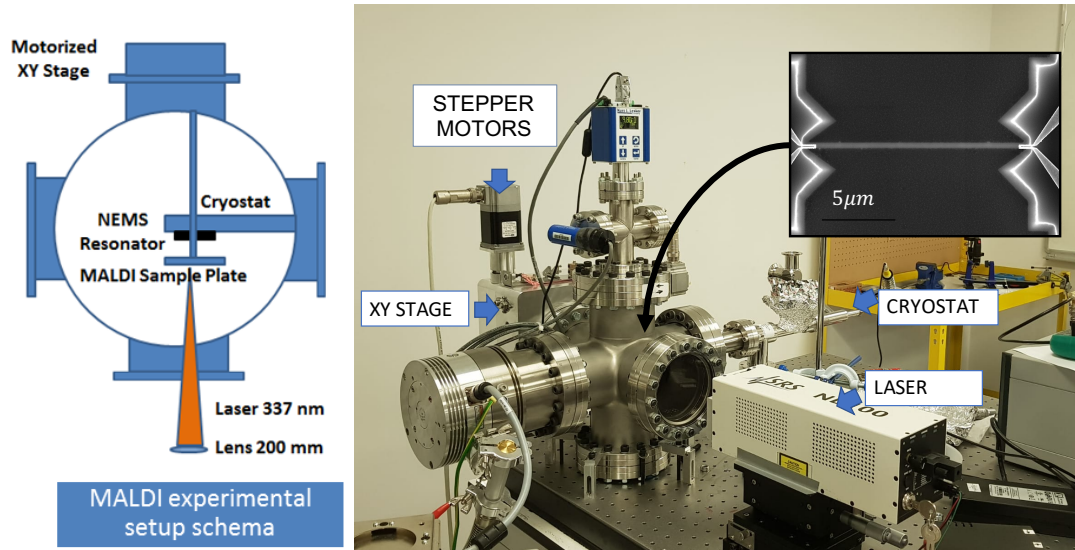


Figure 4.1: (a) Schema of Experimental setup from top view. (b) Photograph of the experimental setup used for MALDI of gold nanoparticles.

For the MALDI experiments with nonlinear NEMS resonators, as a first step, commercially available 20 nm Gold Nanoparticle (GNP) solution from Sigma-Aldrich (Product No: 741965) was dripped on a thin (200 micron) glass slide and left to dry. After the solution dries out, the glass slide is placed into vacuum chamber. Then NEMS resonator is mounted on a flow cryostat and placed into vacuum chamber. The glass slide and the NEMS resonator faces each other inside the vacuum. The mounter which holds the glass slide is connected to the stepper motors from outside the vacuum chamber which enables us to move the glass in  $x$  and  $y$  directions. In this way, we can scan over the glass while the laser is kept fixed at the point close to the resonator. For the MALDI operation, we used NL 100 nitrogen laser (Stanford Research Systems). IT has 337 nm wavelength and

176 micro Joule per pulse laser energy. To increase the focus at a single point, laser focusing lens is mounted in front of the laser beam shutter. Moreover, laser is placed on XYZ micrometer stage to adjust the laser beam towards NEMS for successful MALDI operation.

## 4.2 Two Mode Sensing with Sequential TLL

The frequency shift caused by an analyte is expected to be larger in the nonlinear regime than its counterpart in the linear regime [45, 58]. However, the normalized frequency shift (absolute frequency shift over the resonance frequency) due to an analyte is expected to be the same in both cases.

The bifurcation frequency at the higher amplitude is defined with the curve;  $f_{up} = f_0 \left( 1 + \frac{1}{\sqrt{3}Q} \left( \frac{a_{up}}{a_c} \right)^2 \right)$  where  $a_c$  is the resonance amplitude at the onset of the nonlinearity,  $f_0$  is the linear resonance frequency. Let's define the  $f'_0$  as the updated linear frequency after a single nanoparticle adsorption. Assuming the quality factor (Q) and  $a_c$  will stay constant after the particle, then we can write:  $f'_{up} = f'_0 \frac{1}{\sqrt{3}Q} \left( \frac{a_{up}}{a_c} \right)^2$ .

In order to verify this equality, we have built a measurement system to sequentially switch between the linear and nonlinear operations, therefore the frequency shifts from the same nanoparticle can be directly compared with each other. We continuously switched between TLL and PLL to observe the nonlinear and linear frequency shifts for a single nano particle (Figure 4.2). In addition, we calculated the fractional shifts for the 10 events in Figure 4.3. The frequency shifts in nonlinear and linear regime demonstrated a good agreement within the measurement uncertainty as it can be seen from the  $f_{down}$  measured by TLL follows the PLL path in Figure 4.2b. Although frequency shifts in the nonlinear regime is expected to be larger than the shifts in the linear regime with  $\frac{1}{Q} \left( \frac{a_{up}}{a_c} \right)^2$ , for our case with very high Q (about 12000), this difference stays below the noise level of frequency measurements.

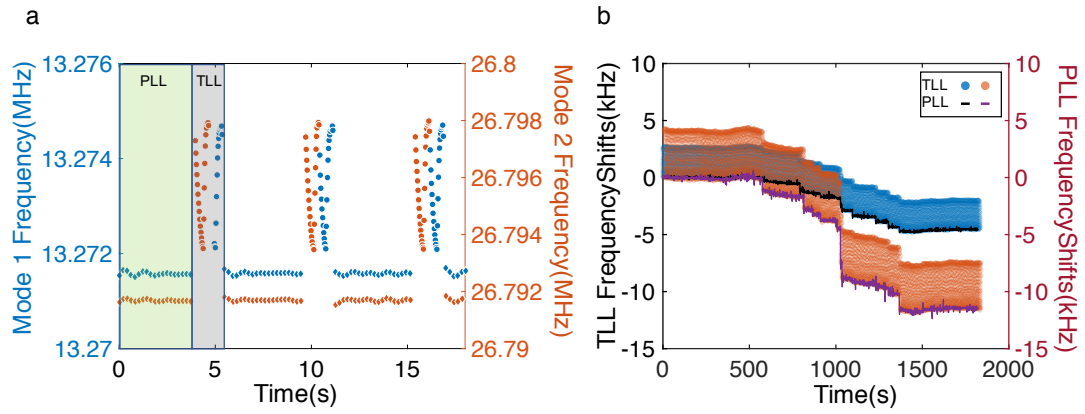


Figure 4.2: Comparison of nano particle induced frequency shifts in nonlinear and linear regime. (a) PLL and TLL are performed consecutively by sequentially switching between the operation regimes. PLL time is set to approximately 4s (shaded green) while the TLL is performed for one full cycle of the first and second mode (shaded grey). (b) While driving the resonator with these technique, 20 nm gold nanoparticle induced frequency shifts are captured for the first two modes of the resonator in linear (solid lines with black (first mode) and purple (second mode)) and nonlinear regime (circle data points with blue (first mode) and orange (second mode)) via PLL and TLL respectively. The TLL frequency jumps are calculated by considering the lowest data point in each cycle, which corresponds to  $f_{down}$ .

| Event No | First Mode                                      |  |                       | Second Mode                                     |  |                       |
|----------|---|--|-----------------------|---|--|-----------------------|
|          | Nonlinear Fractional Shifts( $\times 10^{-4}$ ) | Linear Fractional Shifts( $\times 10^{-4}$ ) | Percentage Difference | Nonlinear Fractional Shifts( $\times 10^{-4}$ ) | Linear Fractional Shifts( $\times 10^{-4}$ ) | Percentage Difference |
| 1        | -0.1642   | -0.1523                                      | 7.25                  | -0.3519   | -0.3482                                      | 1.05                  |
| 2        | -0.2682   | -0.2702                                      | 0.75                  | -0.5126   | -0.5058                                      | 1.33                  |
| 3        | -0.1068   | -0.1037                                      | 2.90                  | -0.4012   | -0.4080                                      | 1.69                  |
| 4        | -0.1077   | -0.1161                                      | 7.80                  | -0.1573   | -0.1569                                      | 0.25                  |
| 5        | -0.3057   | -0.3096                                      | 1.28                  | -0.1628   | -0.1621                                      | 0.43                  |
| 6        | -0.0631   | -0.0689                                      | 9.19                  | -0.2102   | -0.2177                                      | 3.57                  |
| 7        | -0.4110   | -0.4062                                      | 1.17                  | 1.1031  | 1.1001                                       | 0.27                  |
| 8        | -0.3511   | -0.3574                                      | 1.79                  | -0.4710   | -0.4860                                      | 3.18                  |
| 9        | -0.3468   | -0.3455                                      | 0.37                  | -0.0925   | -0.0983                                      | 6.27                  |
| 10       | -0.3104   | -0.3095                                      | 0.29                  | -0.0699   | -0.0667                                      | 4.58                  |

Figure 4.3: Single nano particle induced fractional frequency shifts are obtained in nonlinear regime by measuring the shifts in  $f_{down}$  and they are compared with the linear fractional shifts for the same particle as it is observed in Figure 4.2

As expected from the theory, the fractional frequency shifts measured by both techniques had resulted in essentially the same values within the measurement uncertainty. Once the feasibility of the technique is thus established, we have used our sensor to characterize the 20 nm GNP solution. Mass spectrometry of the individual gold nanoparticles is performed by using matrix-assisted laser desorption ionization (MALDI) method [6], also explained in the previous section. Figure 4.4 demonstrates the snapshot of the two-mode sequential TLL data during the MALDI deposition of gold nanoparticles. Although it looks very similar to the PLL data at first glance, inset discloses the curved TLL data traces.

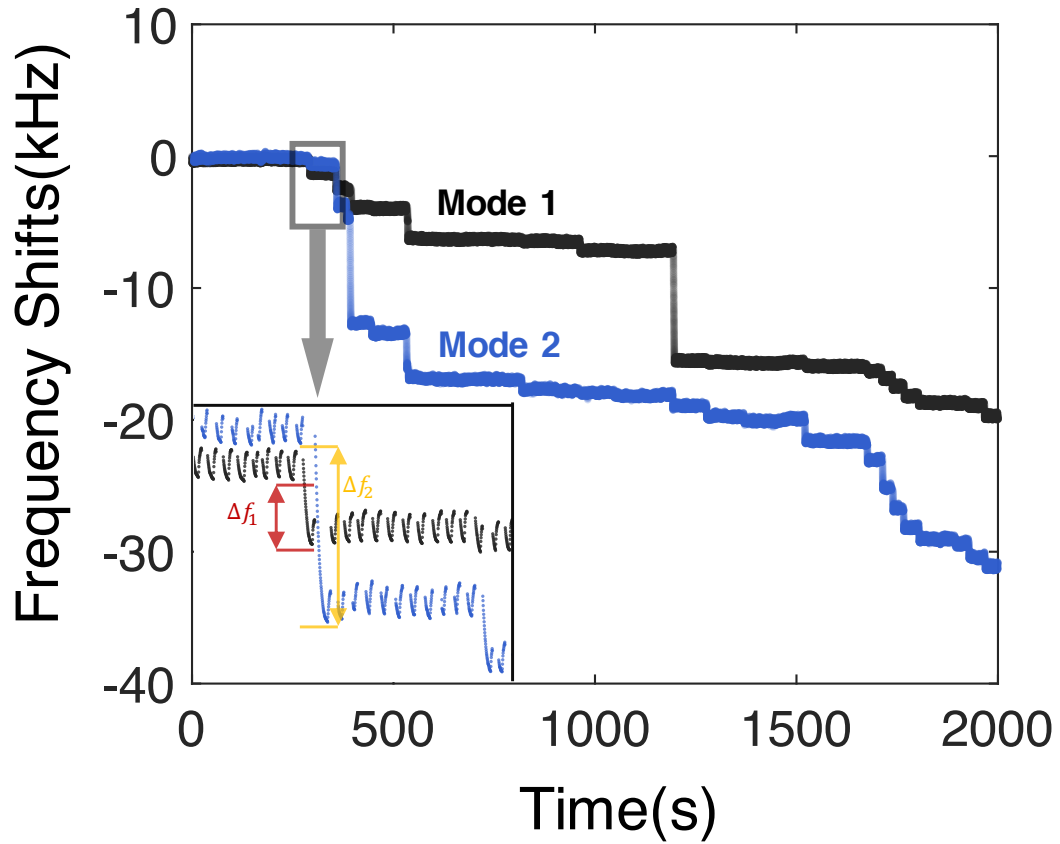


Figure 4.4: Gold nanoparticle (GNP) sensing with Sequential TLL. The frequency shifts due to individual GNP deposition. Each GNP adsorption causes frequency shifts in both modes, which emerge as sudden shifts in the trajectories (inset).

### 4.3 Mass Spectrometry of 20nm Gold Nanoparticles

For the validation of the proposed method for mass sensing, we used normalized frequency shift of the lower bifurcation point ( $f_{down}$ ) since it has a smaller noise level (as expected from [45] and also shown in Chapter 3). As the normalized

frequency shifts in nonlinear regime are shown to be same with the linear sensing, the earlier formulation for converting two-mode frequency shifts to the mass and position values [6], 40 may directly be reused in this case. In Figure 4.5, we present mass spectra for 500 gold nanoparticles with a nominal diameter of 20 nm (12% dispersion in size) obtained by projecting the individual mass distributions onto the mass and diameter planes. For the mass measurements, the peak with maximum probability density is found at 57.25 MDa which corresponds to a diameter of 20.84 nm. The mean value of the gold nanoparticle sample is measured as 26.14 nm with a standard deviation of 5.73 nm. As evident from the mass spectrum, as well as the SEM image shown in Figure 4.6, a small portion of the nanoparticles have coalesced either in the solution or on the MALDI plate. For this reason, the mass distribution shows a fat tail with a few outliers on the high-end of the spectrum with a combined effect of shifting the statistical average of the mass distribution to a value higher than the nominal value.

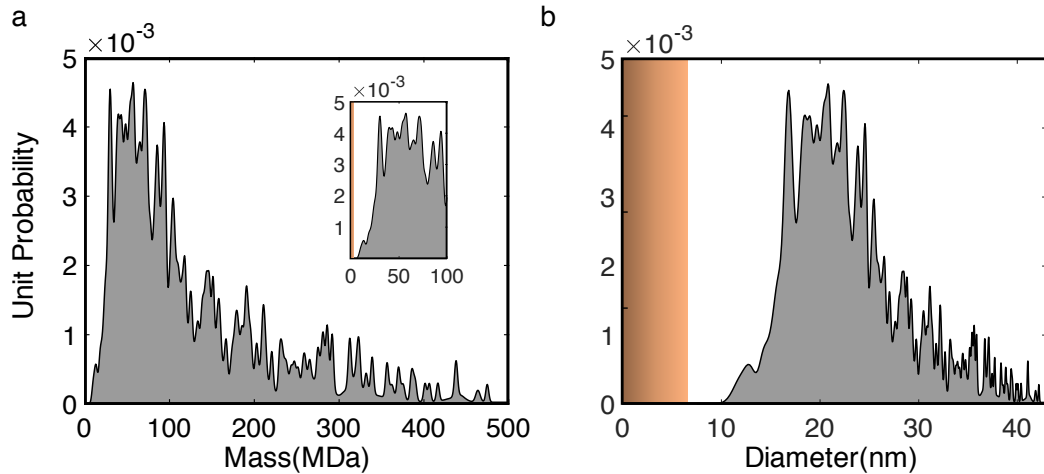


Figure 4.5: (a) Mass spectrometry of 20 nm gold nanoparticles. (b) Diameter is calculated with the bulk density of gold ( $\rho_{Au} = 19.3\text{g/cm}^3$ ). Orange-shaded regions illustrate the detection criterion due to frequency fluctuations of the nonlinear resonator used in the experiments (by assuming the responsivity of the first mode and considering a particle landing at the very center).

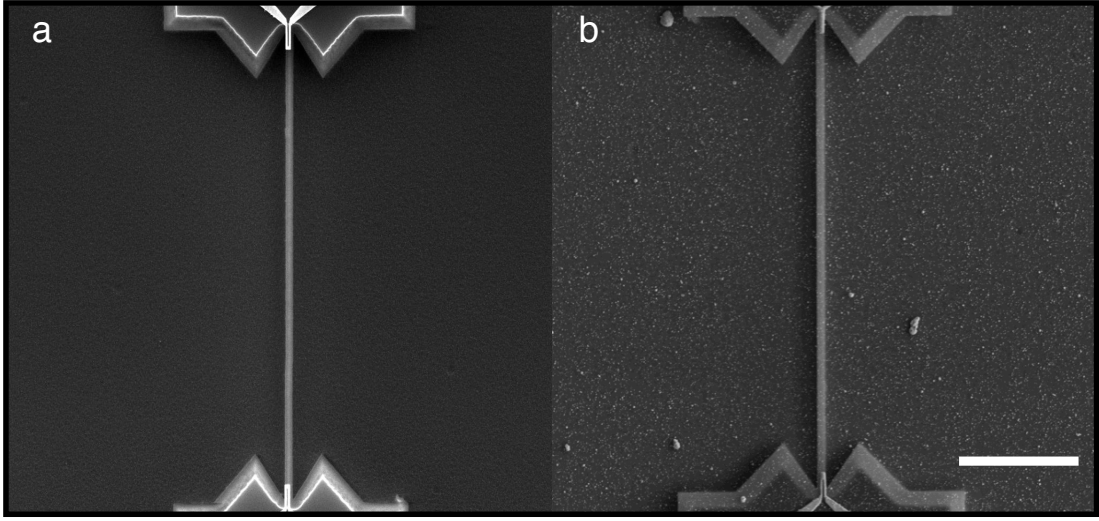


Figure 4.6: SEM images of the 20 micron doubly-clamped beam resonator used for nonlinear mass spectra before (a) and after (b) MALDI process of the gold nanoparticles. Scale bar is 5 micron.

We also note that another advantage of using nonlinear resonators for mass sensing is to increase the maximum measurable frequency shifts compared to PLL. In PLL, frequency shifts larger than half the bandwidth of the resonator induces a phase response outside the resonance feature and causes the controller to lose the phase-locking and frequency traction since in this case the system is translated outside the smooth phase-frequency transition, and the control action is determined by the noise/background at that point, which means that there is no guarantee for phase-locking. In earlier experiments, e.g. with carbon nanotubes, such occurrences were observed [22]. For the TLL however, the acquisition range for the controller is augmented by the width of the hysteresis window. Therefore, the maximum measurable mass increases as the sensor is operated deeper inside the nonlinear regime increases. Although the noise floor also increases in this regime, the dynamic range for mass detection (maximum/minimum detectable masses) keeps increasing. Actually, the largest events in the mass spectra would not have been measurable with a PLL, as the induced frequency shifts were larger than the linear bandwidth of the sensor. TLL provides the freedom to increase the maximum measurable mass (mass ceiling). TLL cycles through the

hysteresis window, which can be made very large by increasing the drive power. For instance, in our TLL GNP data, there are events with very large mass values: such frequency shifts would have kicked a PLL out of its acquisition range which is half of the bandwidth of the resonator.

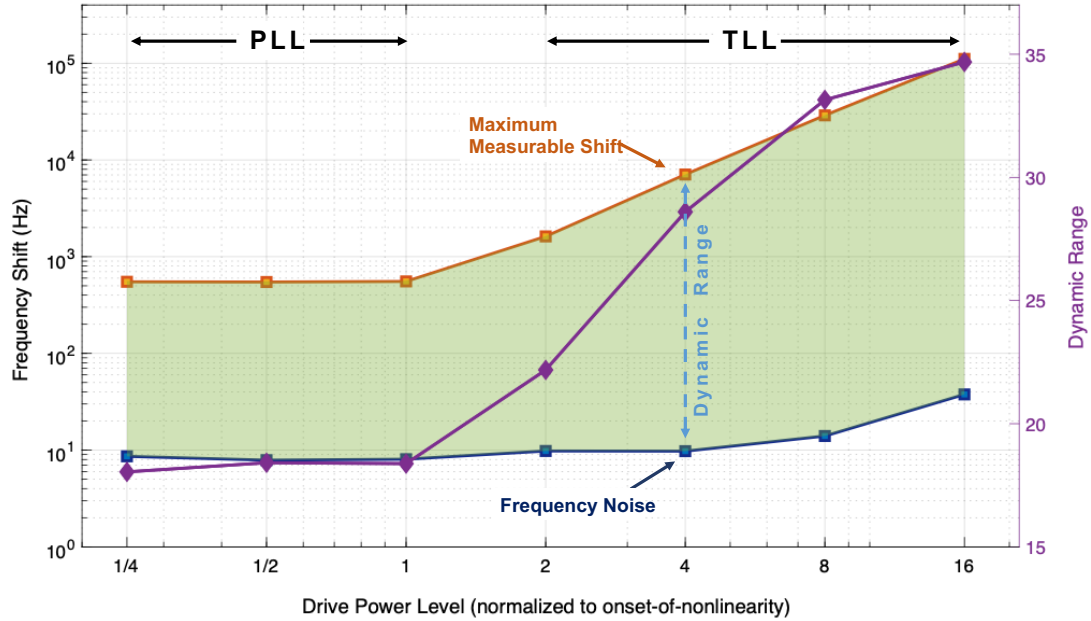


Figure 4.7: Dynamic range comparison between linear and nonlinear regime for mass sensing with PLL and TLL.

In order to compare the mass spectra in the linear regime with the spectra in the nonlinear regime, first we tried to perform MALDI with two-mode simultaneous PLL with the same 20 micron long device. However, the device has small bandwidth (1kHz) in its linear regime which caused phase locked loop system to fail for the analytes that induces a frequency shift larger than half of the bandwidth ( $\frac{f_0}{2Q}$ ). In this case the system is translated outside the smooth phase-frequency transition (Figure 3.1b), and the control action is determined by the noise/background at that point, which means that there is no guarantee for phase-locking. Figure 4.8 demonstrates the failed PLL for the first mode due to large particle landing.

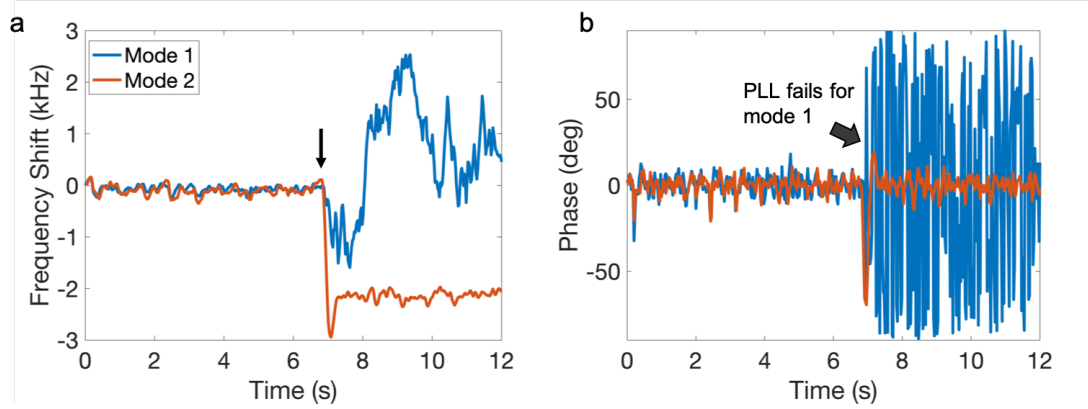


Figure 4.8: An instance when the first mode PLL fails due to a large frequency shift around  $t = 7s$ . (a) PLL simultaneously tracks the first and second mode frequencies in the linear regime. Arrow indicates the moment when the particle lands. Second mode PLL stays phase locked while the first mode PLL fails. (b) Phase response during PLL. After failure for the first mode, phase response is kicked out of the resonance phase transition which results in high errors.

Figure 4.9 shows some of the large frequency shifts that would have kicked PLL out of locking range but were successfully detected by the TLL.

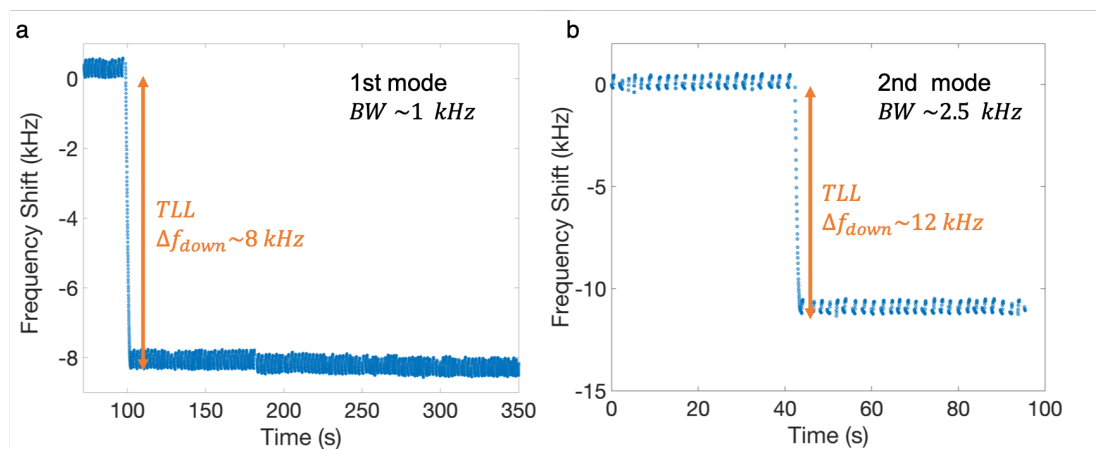


Figure 4.9: Two different instances where TLL detects frequency shifts much larger than the linear bandwidth of the resonator, for the (a) first, and (b) second modes.

In order to avoid this issue, we had to use a slightly different resonator (one with a smaller Q) so that the larger GNPs will not kick the PLL out of the lock-in range.

Mass spectrum of the same GNP sample was also obtained with a NEMS working in the linear regime under PLL in Figure 4.10. Both techniques resulted in very similar mass spectrum graphs. The sample mean and standard deviation in each case were very similar (Figure 4.11). Same gold nanoparticle solution is used for both experiments.

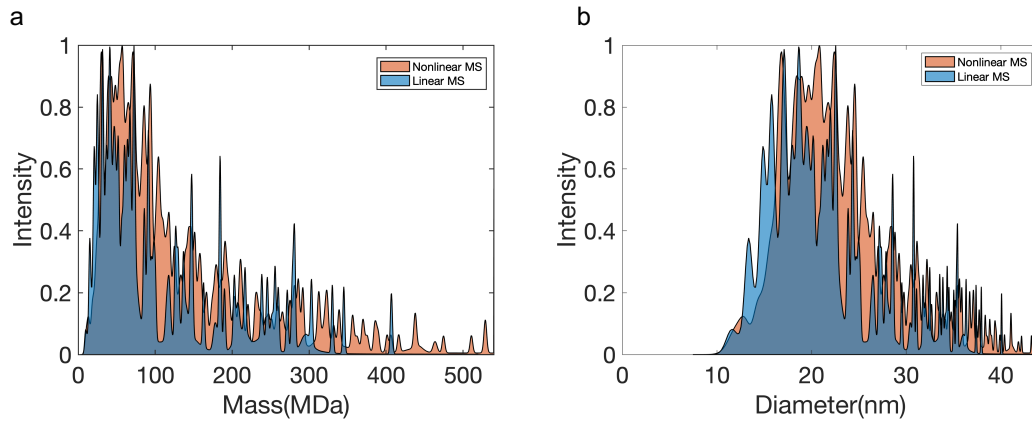


Figure 4.10: Nonlinear and linear mass spectrum are compared. Nonlinear data is the same with the Figure 4.5. Mass spectra (a) and diameter spectra (b) with the assumption of bulk gold density are provided.

| Technique     | Mean diameter $\langle r \rangle$ | Standard Deviation in diameter, $\sigma$ |
|---------------|-----------------------------------|--|
| Linear PLL    | 24.5 nm                           | 5.69 nm                                  |
| Nonlinear TLL | 26.1 nm                           | 5.73 nm                                  |

Figure 4.11: Results from linear and nonlinear mass spectrum.

# Chapter 5

## Concluding Remarks

In this thesis, we present a rapid and accurate method with a feedback controller for trapping the nonlinear resonator alongside the regime of bistability (TLL). By this technique, we can conveniently and precisely track the bifurcation frequencies. Later, we use TLL to characterize the frequency instabilities at these bifurcation points for different averaging times by calculating the Allan deviations. Unlike the linear dynamic range, the nonlinear region does not restrict the amplitude of the resonance at critical amplitude, therefore we further analyze the frequency fluctuations at much larger amplitudes. After we adjust the control and nonlinearity parameters for the nonlinear resonator, we test the feasibility of TLL for the single particle sensing. Results validate that TLL shows a remarkable performance for determining the frequency shifts due to adsorbed particles, therefore can be used for mass spectrometry applications within the nonlinear regime of the NEMS resonators.

Nonlinearity in NEMS resonators has long been acknowledged as a resource, however, its usage in sensing applications has generally been avoided due to the complexity of feedback circuits. Whereas, PLL systems have provided a means for frequency tracking of linear resonators rapidly which was absent in the nonlinear region until now. We demonstrated that a feedback controller similar to PLL—but circulating between two points rather than locking onto a point—can be

used for reliable frequency tracking in nonlinear response.

NEMS resonators have been shrinking in size— a trend which will result in a reduced, and even nonexistent, linear dynamic range. The performance of inherently nonlinear resonators for single particle and molecule detection is still unknown due to the lack of robust techniques for enabling nonlinear frequency tracking. Our method can be deployed on such systems rather effortlessly and help us further analyze the potential of nonlinearity in NEMS sensors. Moreover, the applicability of the method is not limited with the mechanical resonators as it can be adjusted to any Duffing resonator.

# Bibliography

- [1] T. Kouh, S. Hanay, and K. L. Ekinici, “Nanomechanical motion transducers for miniaturized mechanical systems,” *Micromachines*, vol. 8, p. 108, 04 2017.
- [2] H. Postma, I. Kozinsky, A. Husain, and M. Roukes, “Dynamic range of nanotube- and nanowire-based electromechanical systems,” *Applied Physics Letters*, vol. 86, pp. 223105 – 223105, 06 2005.
- [3] D. Rugar, R. Budakian, H. Mamin, and B. Chui, “Single spin detection by magnetic resonance force microscopy,” *Nature*, vol. 430, pp. 329–32, 08 2004.
- [4] J. Chaste, A. Eichler, J. Moser, G. Ceballos, R. Rurali, and A. Bachtold, “A nanomechanical mass sensor with yoctogram resolution,” *Nature nanotechnology*, vol. 7, pp. 301–4, 04 2012.
- [5] A. Naik, S. Hanay, W. Hiebert, P. Feng, and M. Roukes, “Toward single-molecule nanomechanical mass spectrometry,” *Nature nanotechnology*, vol. 4, pp. 445–50, 08 2009.
- [6] S. Hanay, S. Kelber, A. Naik, D. Chi, S. Hentz, E. Bullard, E. Colinet, L. Duraffourg, and M. Roukes, “Single-protein nanomechanical mass spectrometry in real time,” *Nature nanotechnology*, vol. 7, pp. 602–8, 08 2012.
- [7] S. Schmid, M. Kurek, J. Adolphsen, and A. Boisen, “Real-time single airborne nanoparticle detection with nanomechanical resonant filter-fiber,” *Scientific reports*, vol. 3, p. 1288, 02 2013.

- [8] E. Sage, A. Brenac, T. Alava, R. Morel, C. Dupré, S. Hanay, L. Duraffourg, C. Masselon, and S. Hentz, “Neutral particle mass spectrometry with nanomechanical systems,” *Nature communications*, vol. 6, 05 2014.
- [9] J. Lee, W. Shen, K. Payer, T. P. Burg, and S. R. Manalis, “Toward attogram mass measurements in solution with suspended nanochannel resonators,” *Nano Letters*, vol. 10, no. 7, pp. 2537–2542, 2010. PMID: 20527897.
- [10] S. Olcum, N. Cermak, S. C. Wasserman, K. S. Christine, H. Atsumi, K. R. Payer, W. Shen, J. Lee, A. M. Belcher, S. N. Bhatia, and S. R. Manalis, “Weighing nanoparticles in solution at the attogram scale,” *Proceedings of the National Academy of Sciences*, vol. 111, no. 4, pp. 1310–1315, 2014.
- [11] S. Hanay, S. Kelber, C. O’Connell, P. Mulvaney, J. E Sader, and M. Roukes, “Inertial imaging with nanomechanical systems,” *Nature nanotechnology*, vol. 10, 03 2015.
- [12] M. Kelleci, H. Aydogmus, L. Aslanbas, S. Erbil, and S. Hanay, “Correction: Towards microwave imaging of cells,” *Lab on a Chip*, vol. 18, 01 2018.
- [13] R. Lifshitz and M. C. Cross, *Reviews of Nonlinear Dynamics and Complexity*, vol. 1, pp. 1 – 52. 01 2008.
- [14] M. Yuksel, E. Orhan, C. Yanik, A. B. Ari, A. Demir, and M. S. Hanay, “Non-linear nanomechanical mass spectrometry at the single-nanoparticle level,” *Nano Letters*, vol. 19, no. 6, pp. 3583–3589, 2019. PMID: 31117750.
- [15] A. B. Ar ı, M. Ç a ğ atay Karakan, C. Yan ık, i. d. I. i. d. I. Kaya, and M. Selim Hanay, “Intermodal coupling as a probe for detecting nanomechanical modes,” *Phys. Rev. Applied*, vol. 9, p. 034024, Mar 2018.
- [16] M. C. Cross and R. Lifshitz, “Elastic wave transmission at an abrupt junction in a thin plate with application to heat transport and vibrations in mesoscopic systems,” *Phys. Rev. B*, vol. 64, p. 085324, Aug 2001.
- [17] I. Bargatin, I. Kozinsky, and M. Roukes, “Efficient electrothermal actuation of multiple modes of high-frequency nanoelectromechanical resonators,” *Applied Physics Letters*, vol. 90, 02 2007.

- [18] M. Sansa, M. Fernández-Regúlez, J. Llobet, A. San Paulo, and F. Pérez-Murano, “High-sensitivity linear piezoresistive transduction for nanomechanical beam resonators,” *Nature communications*, vol. 5, p. 4313, 07 2014.
- [19] I. Bargatin, E. B. Myers, J. Arlett, B. Gudlewski, and M. L. Roukes, “Sensitive detection of nanomechanical motion using piezoresistive signal down-mixing,” *Applied Physics Letters*, vol. 86, no. 13, p. 133109, 2005.
- [20] K. Jensen, K. Kim, and A. Zettl, “An atomic-resolution nanomechanical mass sensor,” *Nature nanotechnology*, vol. 3, pp. 533–7, 10 2008.
- [21] B. Lassagne, D. Garcia-Sanchez, A. Aguasca, and A. Bachtold, “Ultrasensitive mass sensing with a nanotube electromechanical resonator,” *Nano Letters*, vol. 8, no. 11, pp. 3735–3738, 2008. PMID: 18939809.
- [22] J. Chaste, A. Eichler, J. Moser, G. Ceballos, R. Rurali, and A. Bachtold, “A nanomechanical mass sensor with yoctogram resolution,” *Nature nanotechnology*, vol. 7, pp. 301–4, 04 2012.
- [23] J. E. Sader, M. S. Hanay, A. P. Neumann, and M. L. Roukes, “Mass spectrometry using nanomechanical systems: Beyond the point-mass approximation,” *Nano Letters*, vol. 18, no. 3, pp. 1608–1614, 2018. PMID: 29369636.
- [24] S. Dominguez, S. Fostner, M. Defoort, M. Sansa, A.-K. Stark, M. Halim, E. Vernhes, M. Gely, G. Jourdan, T. Alava, P. Boulanger, C. Masselon, and S. Hentz, “Neutral mass spectrometry of virus capsids above 100 megadaltons with nanomechanical resonators,” *Science*, vol. 362, pp. 918–922, 11 2018.
- [25] M. Li, H. Tang, and M. Roukes, “Ultra-sensitive nems-based cantilevers for sensing, scanned probe and very high-frequency applications,” *Nature nanotechnology*, vol. 2, pp. 114–20, 02 2007.
- [26] A. Peschot, C. Qian, and T.-J. King Liu, “Nanoelectromechanical switches for low-power digital computing,” *Micromachines*, vol. 6, pp. 1046–1065, 08 2015.

- [27] P. Ivaldi, J. Abergel, M. Matheny, L. G. Villanueva, R. B Karabalin, M. Roukes, P. Andreucci, S. Hentz, and E. Defay, “50 nm thick aln film-based piezoelectric cantilevers for gravimetric detection,” *Journal of Micromechanics and Microengineering*, vol. 21, p. 085023, 07 2011.
- [28] J. S. Bunch, A. M. van der Zande, S. S. Verbridge, I. W. Frank, D. M. Tanenbaum, J. M. Parpia, H. G. Craighead, and P. L. McEuen, “Electromechanical resonators from graphene sheets,” *Science*, vol. 315, no. 5811, pp. 490–493, 2007.
- [29] C. Chen, S. Rosenblatt, K. Bolotin, W. Kalb, P. Kim, I. Kymissis, H. L Stormer, T. Heinz, and J. Hone, “Performance of monolayer graphene nanomechanical resonators with electrical readout,” *Nature nanotechnology*, vol. 4, pp. 861–7, 09 2009.
- [30] A. Eichler, J. Moser, J. Chaste, M. Zdrojek, I. Wilson-Rae, and A. Bachtold, “Nonlinear damping in mechanical resonators made from carbon nanotubes and graphene,” *Nature nanotechnology*, vol. 6, pp. 339–42, 05 2011.
- [31] C. Samanta, N. Arora, and A. Naik, “Tuning of geometric nonlinearity in ultrathin nanoelectromechanical systems,” *Applied Physics Letters*, vol. 113, p. 113101, 09 2018.
- [32] J. Gieseler, L. Novotny, and R. Quidant, “Thermal nonlinearities in a nanomechanical oscillator,” *Nature Physics*, 07 2013.
- [33] W. J. Venstra, H. J. R. Westra, and H. S. J. van der Zant, “Mechanical stiffening, bistability, and bit operations in a microcantilever,” *Applied Physics Letters*, vol. 97, 11 2010.
- [34] I. Kozinsky, H. Postma, I. Bargatin, and M. Roukes, “Tuning nonlinearity, dynamic range, and frequency of nanomechanical resonators,” *Applied Physics Letters*, vol. 88, pp. 253101 – 253101, 07 2006.
- [35] J. Lee, Z. Wang, K. He, R. Yang, J. Shan, and P. X.-L. Feng, “Electrically tunable single- and few-layer mos2 nanoelectromechanical systems with broad dynamic range,” *Science Advances*, vol. 4, no. 3, 2018.

- [36] M. , E. Sage, E. C. Bullard, M. Gely, T. Alava, E. Colinet, A. Naik, L. G. Villanueva, L. Duraffourg, M. Roukes, G. Jourdan, and S. Hentz, “Frequency fluctuations in silicon nanoresonators,” *Nature Nanotechnology*, vol. 11, 06 2015.
- [37] B. Yurke, D. S. Greywall, A. N. Pargellis, and P. A. Busch, “Theory of amplifier-noise evasion in an oscillator employing a nonlinear resonator,” *Phys. Rev. A*, vol. 51, pp. 4211–4229, May 1995.
- [38] E. Kenig, M. C. Cross, R. Lifshitz, R. B. Karabalin, L. G. Villanueva, M. H. Matheny, and M. L. Roukes, “Passive phase noise cancellation scheme,” *Phys. Rev. Lett.*, vol. 108, p. 264102, Jun 2012.
- [39] C. Chen, D. H. Zanette, J. R. Guest, D. A. Czaplewski, and D. López, “Self-sustained micromechanical oscillator with linear feedback,” *Phys. Rev. Lett.*, vol. 117, p. 017203, Jul 2016.
- [40] A. Demir and M. S. Hanay, “Numerical analysis of multidomain systems: Coupled nonlinear pdes and daes with noise,” *IEEE Transactions on Computer-Aided Design of Integrated Circuits and Systems*, vol. 37, pp. 1445–1458, July 2018.
- [41] V. Kumar, J. W. Boley, Y. Yang, H. Ekowaluyo, J. K. Miller, G. T.-C. Chiu, and J. F. Rhoads, “Bifurcation-based mass sensing using piezoelectrically-actuated microcantilevers,” *Applied Physics Letters*, vol. 98, no. 15, p. 153510, 2011.
- [42] R. L. Harne and K. W. Wang, “Robust sensing methodology for detecting change with bistable circuitry dynamics tailoring,” *Applied Physics Letters*, vol. 102, no. 20, p. 203506, 2013.
- [43] W. J Venstra, M. Capener, and S. R Elliott, “Nanomechanical gas sensing with nonlinear resonant cantilevers,” *Nanotechnology*, vol. 25, p. 425501, 09 2014.
- [44] M. Sansa, V. Nguyen, S. Baguet, C. Lamarque, R. Dufour, and S. Hentz, “Real time sensing in the non linear regime of nems resonators,” in *2016*

*IEEE 29th International Conference on Micro Electro Mechanical Systems (MEMS)*, pp. 1050–1053, Jan 2016.

- [45] O. Maillet, X. Zhou, R. R. Gazizulin, R. Ilic, J. M. Parpia, O. Bourgeois, A. D. Fefferman, and E. Collin, “Measuring frequency fluctuations in non-linear nanomechanical resonators,” *ACS Nano*, vol. 12, no. 6, pp. 5753–5760, 2018. PMID: 29733575.
- [46] M. V. Requa and K. L. Turner, “Precise frequency estimation in a micro-electromechanical parametric resonator,” *Applied Physics Letters*, vol. 90, no. 17, p. 173508, 2007.
- [47] C. B. Burgner, K. Turner, N. Miller, and S. Shaw, “Parameter sweep strategies for sensing using bifurcations in mems,” 01 2010.
- [48] Z. Yie, M. A. Zielke, C. B. Burgner, and K. Turner, “Comparison of parametric and linear mass detection in the presence of detection noise,” *J. Micromech. Microeng. J. Micromech. Microeng*, vol. 2132, pp. 25027–5, 02 2011.
- [49] J. Rhoads, S. Shaw, and K. Turner, “Nonlinear dynamics and its applications in micro- and nanoresonators,” *Birck and NCN Publications*, vol. 132, 01 2008.
- [50] A. Bouchaala, N. Jaber, O. Yassine, O. Shekhah, V. Chernikova, M. Eddaoudi, and M. Younis, “Nonlinear-based mems sensors and active switches for gas detection,” *Sensors*, vol. 16, p. 758, 05 2016.
- [51] S. Dohn, W. Svendsen, A. Boisen, and O. Hansen, “Mass and position determination of attached particles on cantilever based mass sensors,” *Review of Scientific Instruments*, vol. 78, no. 10, p. 103303, 2007.
- [52] S. Schmid, S. Dohn, and A. Boisen, “Real-time particle mass spectrometry based on resonant micro strings,” *Sensors (Basel, Switzerland)*, vol. 10, pp. 8092–100, 09 2010.
- [53] M. H. Matheny, L. G. Villanueva, R. B. Karabalin, J. E. Sader, and M. L. Roukes, “Nonlinear mode-coupling in nanomechanical systems,” *Nano Letters*, vol. 13, no. 4, pp. 1622–1626, 2013. PMID: 23496001.

- [54] H. J. R. Westra, M. Poot, H. S. J. van der Zant, and W. J. Venstra, “Non-linear modal interactions in clamped-clamped mechanical resonators,” *Phys. Rev. Lett.*, vol. 105, p. 117205, Sep 2010.
- [55] A. Eichler, M. del Álamo Ruiz, J. A. Plaza, and A. Bachtold, “Strong coupling between mechanical modes in a nanotube resonator,” *Phys. Rev. Lett.*, vol. 109, p. 025503, Jul 2012.
- [56] P. A. Truitt, J. B. Hertzberg, E. Altunkaya, and K. C. Schwab, “Linear and nonlinear coupling between transverse modes of a nanomechanical resonator,” *Journal of Applied Physics*, vol. 114, no. 11, p. 114307, 2013.
- [57] R. B Cole, *Electrospray and MALDI Mass Spectrometry*. 01 2010.
- [58] M. D. Dai, K. Eom, and C.-W. Kim, “Nanomechanical mass detection using nonlinear oscillations,” *Applied Physics Letters*, vol. 95, no. 20, p. 203104, 2009.

# Appendix A

## Matlab Code for TLL

```
% PLL with HF2LI

% Allan deviation analysis with different drive amplitudes

clear

device = 'dev1337';

drive_amp = 0.06;

for i = 1:length(drive_amp)

filename = strcat( num2str(drive_amp(i)),
'_1stmode_belowatm.mat');
```

```

ziDAQ('setDouble', '/dev1337/sigouts/0/
amplitudes/1', drive_amp(i));

%      [phase_up, phase_down, kp] = adjust_phase();

phase_up = 48;

phase_down = -15;

nems1 = ziDAQ('getSample', ['/' device '/demods/0
/sample']);

kp = 700;

ki = 0;

error = 0;

total_error = 0;

f_start = nems1.frequency/2;

tc = 10e-3;

f_old = f_start;

index = 1;

```

```

t_count =0;

while (index < 28000)

nems1 = ziDAQ('getSample',[ '/' device '/demods/
0/sample ']);

[phase1 r1]=cart2pol(nems1.x, nems1.y);

error = phase1;

phase1=57.2957795*phase1;

total_error = total_error + error;

if phase1 > 0

f_new = (0.8*error*kp*abs((phase_up-phase1)/phase_up)
+ total_error*ki) + f_old;

else

f_new = (error*kp*abs((phase_down-phase1)/phase_down)
+ total_error*ki) + f_old;

end

ziDAQ('setDouble', '/dev1337/oscs/0/freq', f_new);

pause(tc*2);

```

```
f_old = f_new;  
  
f(index) = f_new;  
  
t(index) = nems1.timestamp;  
  
r(index) = r1;  
  
phase(index) = phase1;  
  
index=index+1;  
  
end  
  
f=double(f);  
  
t =double(t);  
  
r=double(r);  
  
phase=double(phase);  
  
poll_data = [f ; t ; r ; phase];  
  
save(filename , 'poll_data ');  
  
end
```

# Appendix B

## Matlab Code for Sequential TLL

```
% PLL with HF2LI
% GNP Sensing with Sequential TLL

clear
device = 'dev1337';

nems1 = ziDAQ('getSample',[ '/' device '
/demods/0/sample ']); % First mode
nems2 = ziDAQ('getSample',[ '/' device '
/demods/2/sample ']); % Second mode

error1 = 0;

f1_start = nems1.frequency/2;
f2_start = nems2.frequency/2;

tc = 10e-3;
f1_old = f1_start;
f2_old = f2_start;
```

```

index1 = 1; index2 = 1;
t_count = 0;
while (index1 < 45000)

% First Mode starts beyond f1_up
% After 2 jumps occur, second mode TLL starts

jumps1 = 0;
dummy_old = -1;
while (jumps1 < 2)
nems1 = ziDAQ('getSample', ['/ ' device '/demods
/0/sample ']);
[phase1 r1] = cart2pol(nems1.x, nems1.y);
error1 = phase1;
phase1 = 57.2957795 * phase1;

if phase1 > 0
f1_new = error1 * kp * abs((phase_up - phase1) / phase_up)
+ f1_old;
dummy_new = 1;
else
f1_new = error1 * kp * abs((phase_down - phase1)
/ phase_down) + f1_old;

dummy_new = -1;
end

if (dummy_old + dummy_new == 0)
jumps = jumps + 1;
end

ziDAQ('setDouble', '/dev1337/oscs/0/freq', f1_new);

```

```

%           pause(tc*1);
f1_old = f1_new;
dummy_old = dummy_new;

f1(index1) = f1_new;
t1(index1) = nems1.timestamp;
r1(index1) = r1;
phase1_write(index1) = phase1;
index1=index1+1;

end

% Second Mode starts beyond f2_up
% After 2 jumps occur, first mode TLL starts again

jumps2 = 0;
dummy_old = -1;

while (jumps2<2)
nems2 = ziDAQ('getSample',[ '/' device '/demods/2/sample ']);
[phase2 r2]=cart2pol(nems2.x, nems2.y);
error2 = phase2;
phase2 = 57.2957795*phase2;

if phase2 > 0
f2_new = error2*kp*abs((phase2_up-phase2)/phase2_up)
+ f2_old;
dummy_new = 1;
else
f2_new = error2*kp*abs((phase2_down-phase2)
/phase2_down) + f2_old;
dummy_new = -1;
end
end

```

```

if (dummy_old + dummy_new == 0)
jumps = jumps+1;
end

ziDAQ('setDouble', '/dev1337/oscs/1/freq', f2_new);
pause(tc*1);
f2_old = f2_new;
dummy_old = dummy_new;

f2(index2) = f2_new;
t2(index2) = nems2.timestamp;
r2(index2) = r1;
phase2_write(index2) = phase2;
index2=index2+1;
end

end

f1=double(f1);
t1 =double(t1);
r1=double(r1);
phase1_write=double(phase1_write);
f2=double(f2);
t2 =double(t2);
r2=double(r2);
phase2_write=double(phase2_write);
poll_data = [f1 ; t1 ; r1 ; phase1_write;
  f2 ; t2 ; r2 ; phase2_write];

```